VARIABIILTY AND PREDICTABILITY OF COLD-SEASON ATMOSPHERIC RIVER ACTIVITY OVER THE NORTH ATLANTIC

Chuxuan Li

A thesis submitted to the faculty at the University of North Carolina at Chapel Hill in partial fulfillment of the requirements for the degree of Master of Science in the Department of Marine Sciences

Chapel Hill
2020

Approved by:

Wei Mei

John M. Bane

Bin Guan

ABSTRACT

Chuxuan Li: Variability and predictability of cold-season atmospheric river activity over the North Atlantic
(Under the direction of Wei Mei)

Atmospheric rivers (ARs) are conduits of enhanced water vapor transport in the lower troposphere and cause extreme precipitation and flooding events in many regions. This thesis explores the variability and predictability of North Atlantic (NA) AR activity using a set of large-ensemble atmospheric simulations and observations. In the first part, we depict three leading modes governing sea surface temperature-forced variability in AR occurrence frequency via an empirical orthogonal function analysis. We then characterize their spatiotemporal variations, determine their physical mechanisms, and link them to large-scale modes of climate variability. We also identify the regions where seasonal AR occurrence has relatively high or low predictability. In the second part, we divide NA ARs into four distinct clusters based on their genesis locations and trajectories, and for each cluster identify the large-scale climate modes controlling the year-to-year variations in its population and the regions vulnerable to its induced extreme precipitation and winds.

ACKNOWLEDGEMENTS

I would like to firstly give my gratitude to my supervisor, Dr. Wei Mei. Thank you for introducing me into the field of climate sciences, a brand-new world to me. Thank you for teaching me how to perform science step by step, and in the meanwhile, leaving me with space to conduct research independently. You taught me to be a tough person, and fortunately now I am more than determined and confident to embrace and overcome new challenges.

I would also want to thank my thesis committee members. Thank you, Dr. John Bane, for leading progress towards my MS degree and for contributing invaluable insights into my research projects. Thank you for always taking care of me and for your utmost guidance and support during my graduate studies. Thank you, Dr. Bin Guan, for providing me with the most professional insights into the atmospheric river science. Although you are far away at UCLA, and we've only met for very few times, I enjoyed the time discussing science with you very much.

Finally, yet importantly, I would like to give my deepest gratitude to my families and friends– my parents and grandparents who raised me, my boyfriend Nuo who unreservedly supports me, my bestie Yiqian who is always there for me, and my roommate Xiaodan who reassures and stimulates me. I am also very happy for the three years spent at UNC-Chapel hill, being grateful for meeting a lot of fantastic mentors and friends here, including Dr. Harvey Seim, Dr. Emily Eidam, Wenjing, Lu, Weihui, Xiluo, and Taylor. I am excited that my journey to an MS degree has come to an end with many works that I am very proud of. These could not be accomplished without any of you — so, many thanks again.

TABLE OF CONTENTS

LIST OF TABLES

LIST OF FIGURES

LIST OF ABBREVIATIONS

AO	Arctic Oscillation
AGCM	Atmospheric general circulation model
AMIP	Atmospheric Model Intercomparison Project
ARTMIP	Atmospheric River Tracking Method Intercomparison Project
ARs	Atmospheric rivers
CMIP	Coupled Model Intercomparison Project
d4PDF	Database for Policy Decision-making of Future climate change
DJFM	December, January, February, and March
ENSO	El Niño–Southern Oscillation
EOF	Empirical orthogonal function
GOM	Gulf of Mexico
IPCC	Intergovernmental Panel on Climate Change
IVT	Integrated water vapor transport
IWV	Integrated water vapor

JRA-55	Japanese 55-year reanalysis
LLJ	Low-level jet
M01	The first member of the ensemble simulations
MJO	Madden Julian Oscillation
MRI	Meteorological Research Institute
NA	North Atlantic
NAE	North Atlantic-European sector
NAO	North Atlantic Oscillation
NAOI	North Atlantic Oscillation index
PC	Principle component
PDF	Probability density function
PDO	Pacific Decadal Oscillation
PNA	Pacific/North American pattern
RCP	Representative concentration pathway
SCAND	Scandinavian pattern
SLP	Sea level pressure

SNR	Signal to noise ratio
SST	Sea surface temperature
TNI	Trans-Niño index
u(v)850	Zonal (meridional) wind at 850 hPa
U.K.	United Kingdom
U.S.	United States
Z200 (500)	Geopotential height at 200 (500) hPa

CHAPTER 1: INTRODUCTION

Atmospheric rivers (ARs) and their structures

ARs are filaments-like features transporting large amounts of water vapor across the midlatitudes. They are characterized by enhanced water vapor transport and strong winds in the lower troposphere. The average moisture flux of ARs is equal to the average discharge of liquid water in 2.6 Amazon Rivers (Ralph et al. 2017b), and they account for more than 90% of the poleward water vapor transport in the global middle to high latitudes (Zhu and Newell 1998). These conduits of water vapor flux were discovered earlier on (e.g., Namias 1939) but were not termed ARs until the end of 20th century (Zhu and Newell 1994). Up until now, there are still alternative terminologies being used – such as 'tropical moisture exports' by Knippertz and Wernli (2010) and 'moisture conveyor belts' by Bao et al. (2006). No matter what names, they all refer to (explicitly or implicitly) these rather long (usually more than 2000 km) and narrow (typically 300-500 km) moisture-rich 'rivers' in the atmosphere (Ralph and Dettinger 2011).

ARs occur most frequently in the midlatitudes. On average, there are 3–5 ARs at any moment in each hemisphere (Zhu and Newell 1998). They are usually embedded within the warm conveyor belts in the pre-cold-frontal regions of extratropical cyclones. The structure of a typical AR is shown in Figure 1.1. Thanks to many observational studies, we now know several important features of an AR (Ralph et al. 2004, 2005): (1) enhanced vertically integrated water vapor (IWV) in a narrow and long band along the cold front, (2) a low-level jet (LLJ) located at around 1 km

above mean sea level in front of the cold front, and (3) moist-neutral stratification in the lower troposphere within the AR.

The impacts of ARs

ARs can have dual impacts. In some regions, they can cause extreme precipitation during landfalls, and hence can induce devastating secondary disasters like landslides, flooding events, etc. (Eiras-Barca et al. 2016; Ralph et al. 2006; Leung and Qian 2009; Neiman et al. 2008b, 2011; Waliser and Guan 2017; Cordeira at al. 2019; Lavers et al. 2011, 2012; Bath et al. 2017). The LLJs associated with ARs, meanwhile, can cause wind damage to people's properties, anomalously high sea levels, coastal flooding, and storm surges at the coasts (Waliser and Guan 2017; Khouakhi and Villarini 2016). At higher elevations, ARs can contribute to the accumulation (Guan et al. 2010, 2013) or ablation (Guan et al. 2016) of the snow-pack in the mountains. On the positive side, ARs can provide crucial water resources to alleviate the situations in drought areas and end drought seasons (Dettinger 2013; Gershunov et al. 2017).

The associations between large-scale climate dynamics and ARs

Large-scale climate variabilities such as El Niño-Southern Oscillation (ENSO), Arctic Oscillation (AO), Pacific Decadal Oscillation (PDO), Pacific-North America (PNA) pattern, North Atlantic Oscillation (NAO), Scandinavian pattern (SCAND), East Atlantic pattern (EA), and Madden Julian Oscillation (MJO), have been documented to be crucial modulators for AR activities (Gershunov et al. 2017; Mundhenk et al. 2016; Bao et al. 2006; Payne et al. 2014; Lavers et al. 2012; Lavers and Villarini, 2013; Eiras-Barca et al., 2016).

There are plenty of studies focused on ARs along the west coast of North America. Gershunov et al. (2017) investigated the interannual-interdecadal variability of ARs along the west coast of North America, and found the three leading modes of landfalling AR activity – according to a canonical correlation analysis – are associated with PDO, eastern Pacific sea surface temperature (SST), and the northeastern Pacific warm 'blob', respectively. Mundhenk et al. (2016) found that both ENSO and MJO play a role in modifying the AR occurrence, and this modification varies by seasons and locations, reinforcing the seasonal cycle under one circumstance while completely offsetting it under another. Bao et al. (2006) argued that enhanced IVT originated from the tropics is most favored during the neutral ENSO condition and is least possible during El Niño. Payne et al. (2014) discovered an equatorward shifted jet during El Niño phase together with equatorward-displaced landfalling ARs. Besides, other dynamics like Rossby wave breaking, East Asian subtropical jet, and Pacific-Japan teleconnections are also suggested modulators for AR activities (Ryoo et al. 2013; Hu et al. 2017; Zhang and Villarini 2017).

While studies above mentioned are focused on North Pacific, similar studies for North Atlantic (NA) are rather sparse. A negative correlation was found between wintertime AR counts and SCAND (Lavers et al. 2012). In addition, positive NAO conditions are associated with AR landfalls in the northern Europe (Lavers and Villarini 2013), while negative NAO and positive EA are proved to be favorable for ARs landfalling to the southern Europe (Eiras-Barca et al. 2016; Brands et al. 2016). As in the proposed 'Mexican connection' that links SST anomalies in the Pacific with circulation anomalies over the western subtropical Atlantic (Rasmusson and Mo 1993), some recent findings also demonstrate that the climate and SST patterns in the Pacific may modulate AR activities in the NA (Strong and Magnusdottir 2008a; Knippertz and Wernli, 2009).

Current knowledge gaps

While a majority of the abovementioned studies are focused on regional ARs along the west coasts of North America and Europe, very few touched on the interannual-decadal variability and predictability of NA AR activities (e.g., occurrence frequency, trajectory, and landfalling locations) from a basin-wide perspective. AR activity over the southeastern U.S. is among the least studied so far. However, it will be proved in this thesis that most of the NA coastlines, especially along the southeastern U.S., are vulnerable to extreme precipitation and strong winds as they are highly-impacted by frequent AR occurrences. Therefore, a more profound understanding about the variability in AR occurrence and tracks and its underlying mechanisms is a prerequisite to ultimately prepare for and mitigate the socioeconomic loss brought by them.

What's more, the variability of large-scale atmospheric circulation over the NA is rather complicated because it not only arises from the SST anomalies in local areas and remotely in other oceans (e.g., the Pacific), but also has a part that is internal to the overlying atmosphere (e.g., NAO). This complexity will impinge upon the AR occurrence and tracks and complicate the NA AR predictions. Hence, to improve the predictive skills of NA ARs, we need to again disentangle the mechanisms driving the variability in AR occurrence and investigate into the potential sources of its predictability.

To help fill the knowledge gaps, we employ large-ensemble simulations with a high-resolution atmospheric general circulation model to examine the SST-forced interannual variability and predictability in NA wintertime AR occurrence frequency in the second chapter. In that part, we depict three leading modes governing SST-forced variability in AR occurrence frequency via an empirical orthogonal function analysis. We then link them to large-scale climate variations and

identify the respective regions where seasonal AR occurrence has relatively high and low predictability.

With the chapter of a comprehensive analysis about AR occurrence, we improve our understanding about how AR occurrence varies from year to year under certain modulations of large-scale climate modes, but we still do not know where these ARs originate and terminate and whether these ARs come from one population. Therefore, in the third chapter, a cluster analysis is performed to investigate the variability and heterogeneities in NA AR tracks and landfalling locations. We divide NA ARs into four distinct clusters based on their genesis locations and trajectories, and for each cluster identify the large-scale climate modes controlling the year-to-year variations in its population and the regions vulnerable to its induced extreme precipitation and winds.

In the last chapter, a summary of the thesis is presented and possible research topics in the future are also discussed.

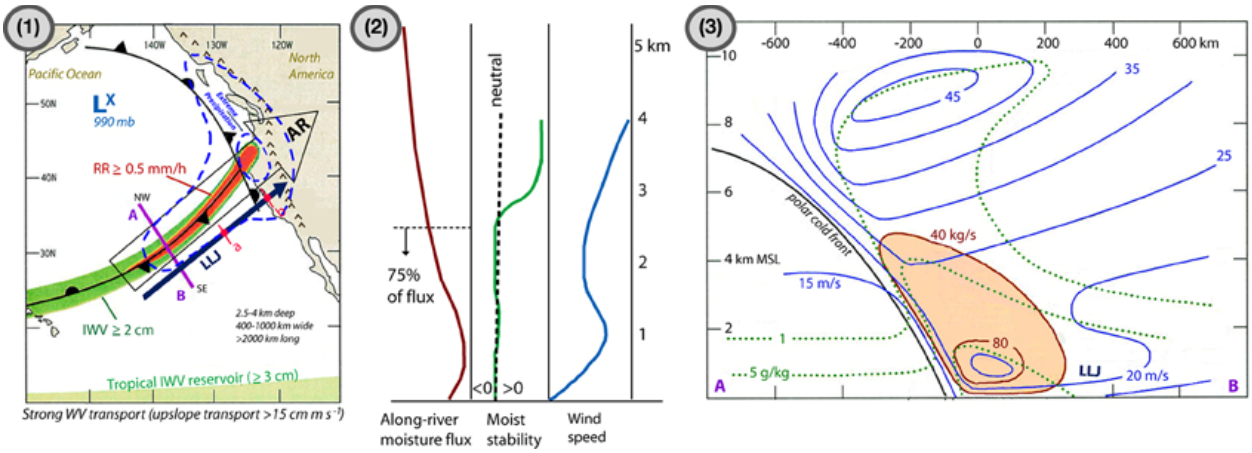

Figure 1.1 The schematic structure of an AR. (1) Plan-view of the AR showing the relative locations of the low-level jet (LLJ), the cold front, the low-pressure center, and the enhanced moisture transport. (2) Vertical structure of moisture flux (in red), moist static stability (in green) and wind speed (in blue) along the LLJ [a–b in (1)]. (3) Cross section schematic through an AR [along A–B in (1)] showing the isotachs (blue contours; m/s), the specific humidity (dotted green contours; g/kg), and the water vapor flux (red contours and shading; kg/s).

(Figure from Gimeno et al. 2014)

CHAPTER 2: THE VARIABILITY AND PREDICTABILITY OF COLD-SEASON ATMOSPHERIC RIVER OCCURRENCE FREQUENCY OVER THE NORTH ATLANTIC

Introduction

Atmospheric rivers (ARs) are filament-like conduits of enhanced water vapor transport in the lower troposphere. Embedded within the warm conveyor belts associated with extratropical cyclones, they occur most frequently over midlatitude oceans. While covering only ~10% of the circumference of Earth over the extratropics, ARs are significant transient features in both global and regional hydrological cycles, accounting for over 90% poleward water vapor transport in the global middle to high latitudes (Zhu and Newell 1998).

Large climate-scale variabilities such as El Niño- Southern Oscillation (ENSO), North Atlantic Oscillation (NAO), Arctic Oscillation (AO), Pacific/North American (PNA) pattern and Pacific Decadal Oscillation (PDO) are suggested to be crucial modulators in AR activities. There are plenty of research directed at modulations on ARs by individual factors in the Pacific and North Atlantic (NA). In North Pacific, a recent Canonical Correlation Analysis shows that PDO is responsible for the AR occurrence along the west coast of North America (Gershunov et al. 2017). El Niño conditions inhibit water vapor transport originating from the tropics (Bao et al. 2006) and shift AR landfalling locations equatorward along the west coast of U.S. (Payne and Magnusdottir 2014). In NA, strong associations have been pointed out between the Scandinavian pattern (SCAND), East Atlantic pattern, and AR counts over various European coastlines (Lavers et al. 2012; Brands et al. 2017). NAO favors landfalling ARs in the southern Europe during its negative

phase (Eiras-Barca et al. 2016), whereas positive NAO conditions are responsible for landfalls in the northern Europe (Lavers and Villarini 2013). As a major source to atmospheric interannual variability over the NA, NAO bears links with SST anomalies in the ENSO region (e.g., Pozo-Vázquez et al. 2001), subtropical Atlantic (e.g., Czaja and Frankignoul 2002) and Indo-west Pacific (Hoerling et al. 2001, 2004; Sanchezgomez et al. 2008; Chu et al. 2017). The teleconnection between climate modes complicates their controls on AR activities and sometimes enables joint modulations. For example, coexisting negative phases of AO and PNA dramatically increase AR occurrence in Sierra Nevada (Guan et al. 2013). In addition, Li and Lau (2012) diagnosed the effect of various combinations of ENSO and NAO phases on transient eddies. However, similar studies for their possible joint modulations on NA ARs seem rather sparse.

Due to the high moisture content they carry with, ARs are important synoptic weather systems that often cause catastrophic precipitation, floods, landslides and other natural hazards in coastal and even inland mountainous areas (Ralph et al. 2006; Leung and Qian 2009; Neiman et al. 2008b, 2011; Waliser and Guan 2017). More than 90% of the anomalous precipitation events over Iberian Atlantic Margin are demonstrated to associate with landfalling ARs in winter (Eiras-Barca et al. 2016), and with orographic uplifting they may cause most severe winter floods in Europe and California (Ralph et al. 2006; Lavers et al. 2011; Lavers et al. 2012; Leung and Qian 2009; Neiman et al. 2011; Bath et al. 2017). As climate change proceeds, intense and persistent AR events will continue to strengthen and become more frequent in many regions (Dettinger 2011; Lavers and Villarini 2013; Lavers et al. 2013; Lavers et al. 2015; Ramos et al. 2016b). Weather forecasting and long-term projection of AR activities (e.g., occurrence, intensity, trajectory, and landfall locations) can provide instructions on policy making, hazard control and water resources management. Hence, the importance of characterizing AR variability, establishing links between

ARs and large-scale climate dynamics, and understanding the internal variability, which will all eventually improve AR predictive skills, cannot be overemphasized.

To address these issues, large-ensemble simulations with a high-resolution atmospheric general circulation model (AGCM) are employed here to investigate the SST-forced NA AR variability and predictability at climate and basin scales. The data and model setup are described in section 2. The climatological AR occurrence is depicted and validated against a reanalysis dataset in the results section. The spatiotemporal patterns, thermodynamic and dynamic components of the three leading modes of the empirical orthogonal function (EOF) of AR occurrence anomalies are then detailed respectively. After that, AR-induced precipitation is examined, which is followed by an anatomy of the internal variability in AR occurrence. The summary section provides a synthesis and discussion of the results, together with an implication for future study.

Data and methods

Observations and reanalysis

To detect ARs over NA from December through March (DJFM) during year 1958-2013, 850 hPa zonal wind (u850) and meridional wind (v850), and specific humidity from 1000 hPa to 300 hPa at 1.25° X 1.25° spatial resolution of the Japanese 55-year Reanalysis (JRA-55) dataset were used. Sea surface temperature (SST) from the COBE SST at 1.0° X 1.0° for 1958-2013 and sea level pressure (SLP) at 1.25° X 1.25° for 1958-2013 from JRA-55 were also used to compare with the variations of AR occurrence to examine the driving mechanisms.

Large-ensemble simulations

The u850, v850, specific humidity and SLP in the Database for Policy Decision-making of Future climate change (d4PDF) were used to examine the interannual variability in AR occurrence during year 1951-2011 and the links to large-scale climate modes. It contains large-ensemble (30-member) simulations performed with a high-resolution model, the Meteorological Research Institute AGCM (MRI-AGCM), version 3.2 (see Mizuta et al. 2012). In the historical runs, MRI-AGCM is driven by observation-based SST, sea ice (Hirahara et al. 2014), and radiative forcing including greenhouse gases, ozone, and aerosols for year 1951-2011. In order to account for uncertainties, each member run was derived by adding SST perturbations, which are determined by the EOFs of the interannual variability in SST, to the best estimate of SST (Hirahara et al. 2014; Mizuta et al. 2017). Such a dataset can be used to analyze how the variability of the atmosphere will respond to prescribed global SST variability. More details about the experimental setup and simulated climate variations can be found in Mizuta et al. (2017) and Kamae et al. (2017).

Detection algorithm of ARs

An AR detection algorithm modified from the original algorithm developed by Mundhenk (2016) is employed to detect ARs from atmospheric fields (see original code in appendix of Mundhenk 2016). In this modified algorithm, we used seven sets of AR criteria including different values of minimum anomalous IVT, length, width, length/width ratio, eccentricity of the fitted ellipse, latitude etc. Anomalous IVT is the anomaly relative to climatology. Elongated object of anomalous water vapor transport is identified as an AR as long as it meets at least one of the seven sets of criteria. Herein, IVT between 1000 and 300 hPa is calculated using 6-hourly specific

humidity and horizontal wind at 1.25° X 1.25° spatial resolution from JRA-55 and d4PDF ensemble simulations respectively following

$$\text{IVT} = \sqrt{(\frac{1}{g}\int_{1000}^{300} qu\ dp)^2 + (\frac{1}{g}\int_{1000}^{300} qv\ dp)^2}\ ,$$

where q is specific humidity, g is the acceleration due to gravity, and u and v are zonal and meridional wind. This detection procedure yields a binary AR occurrence field for each 6-hour time step during 1951-2011. The monthly AR occurrence is generated by summing up the 6-hourly binary occurrence for each month, which is then averaged from December through March to obtain the DJFM mean AR occurrence. Next, we derived the area-weighted AR occurrence anomalies by subtracting the climatology from it and multiplying it by the square root of the cosine of latitude at each grid point. After that, an EOF analysis is conducted to the area-weighted anomalies over the NA (108°W-60°E, 0-80°N) to examine cold-season AR variability. The dominant EOF modes are insensitive to the adjustments of domain. The first three leading modes altogether explain a large proportion of (80%) the total interannual variability, and hence hereafter only these three modes are discussed.

Definition of large-scale climate indices

Niño 3.4 index is the standardized seasonal mean of SST anomalies averaged over 5°S-5°N, 170°W-120°W. Niño 1+2 is averaged over 0-10°S, 90°W-80°W and Niño 4 over 5°S-5°N, 160°E-150°W. Trans-Niño index (TNI) is standardized Niño 4 minus Niño 1+2. NAO and SCNAD indices are represented by the time series of the first two leading principle components of DJFM SLP anomalies over the NA basin (20-80°N, 90°W-40°E), respectively. PNA index is defined by the time series of the first principle component of DJFM geopotential height at 500 hPa (Z500) over 20-80°N, 180°E-60°W. SST is averaged over 40-115°E, 16°S-16°N to represent the Indian

ocean average SST. The time series of the principle components herein are measured in unit of their respective standard deviations. The same calculations for these dynamic indices are carried out for 30 individual members, the ensemble mean, and JRA-55.

Results

Climatology of DJFM AR frequency

The climatological distribution of DJFM AR frequency in the ensemble mean during year 1951-2011 exists to the south of the storm tracks with a southwest-northeast orientation as shown in Figure 2.1a. The frequency at a specific grid cell is calculated as the ratio of the number of 6-hourly time steps with the existence of AR conditions to the total number of time steps during DJFM from 1951-2011. It can also be regarded as an estimate of the likelihood that an AR would occur at any time during winter at a certain location. As shown in Figure 2.1a, AR occurs most frequently over central-western NA at around 30-50°N, where an AR occurs about once every five days (20%) on average during cold season. As high as 17% of the wintertime in Florida State and 10-12% in western Europe experience AR events. While most frequent over ocean, ARs also penetrate far over lands. Central America to New England and southeastern Canada have AR occurrence close to western Europe (10-12%). The value of AR occurrence in this study is slightly higher than those reported by others (e.g., Figure 7a in Guan and Waliser, 2015) because a composite of seven sets of different criteria employed here identifies ARs that would sometimes be missed by e.g., using a single set. Compared to the reanalysis, AR numbers over North Carolina, South Carolina, and Georgia are slightly overestimated in the simulations. Except that, in general, the ensemble mean captures the main features such as the distribution and magnitude of the climatology of wintertime AR occurrence in JRA-55 (Figure 2.1b), confirming that the ensemble

mean has the capability to simulate a realistic AR climatology, which is a manifestation of the model's skills in simulating the mean states of dynamic and thermodynamic fields. To investigate the SST-forced variability of AR occurrence, detailed analyses are focused on the ensemble mean in the following sections.

EOF1 in ensemble mean (a north-south wobbling)

EOF1 of DJFM AR occurrence in the ensemble mean is a dipolar structure characterized by a north-south wobbling from year to year (Figure 2.2a), which accounts for 61.35% of the total interannual variability. With the sign we determined here, the positive phase represents an equatorward shift of AR events, while the negative phase indicates a poleward displacement. During positive PC1 (black line in Figure 2.2b), the northern lobe of the dipole extending from the central U.S. to offshore eastern Canada tends to experience fewer ARs; meanwhile, more ARs can be seen over the Gulf of Mexico (GOM) to central-eastern subtropical NA. These parallel strip-like counterparts spread in a southwest-northeast direction with maximum loadings over east coast of U.S. The negative phase of EOF1, in contrast, exhibits the opposite features.

To examine the physical mechanisms, AR transports are divided into thermodynamical (i.e. specific humidity) and dynamical (i.e. wind circulation) components. Anomalous integrated water vapor (IWV) and low-level wind speed (including u850 and v850), representing the thermodynamic and dynamic components of ARs, are regressed onto AR PC1, yielding an evident tripole pattern in both regressed fields (Figure 2.2 c&d). Since ARs only occasionally occur south of 20°N, the strong variability within the southernmost branch of the tripole in both regressed fields shall not be interpreted as contributing to AR variability. Instead, they originate from the inherent variations in water vapor content and near-surface wind in the tropical-subtropical

Atlantic independent of ARs and hence are beyond the scope of our study. The northern two branches closely mimic the dipolar structure in AR occurrence EOF1. During positive PC1, southward-shifted positive IWV anomalies and westerlies strengthen the IVT over the Gulf Coast and central NA, and suppress IVT over the central U.S. to the east coast of Canada. These changes together shift AR occurrence equatorward. During years of negative PC1, however, mirrored opposites to the positive phase in IWV and wind field will eventually contribute to poleward shifted ARs, impacting the central U.S. to New England.

EOF1 is modulated by several large-scale climatic circulations including ENSO, and NAO (Table 2.1), of which ENSO and PNA are the dominant factors. Niño 3.4 and PNA are highly correlated with PC1, and each accounts for about 81% of its variance (Table 2.1). The NAO index (NAOI) is negatively correlated with PC1 (r=-0.60). In the correlation map between PC1 and global SST, pronounced values are found in Niño 3.4 region (Figure 2.2e, shaded); when correlating PC1 with SLP, a characteristic PNA pattern and a westward-shifted NAO-like pattern are seen over the Pacific-NA sector (Figure 2.2e, black contours). Diabatic heating stemmed from El Niño-related SST excites a wave train structure reminiscent of a PNA pattern (Horel and Wallace 1981). The wave train extends farther eastward into western Europe in the atmospheric model (consistent with Cassou and Terray 2001), and projects onto a westward-shifted negative phase of NAO over NA (Figure 2.2e).

The abovementioned climate patterns also exert joint modulations on NA AR activities. By subtracting NAOI from normalized Niño 3.4, a new index is formed (red line in Figure 2.2b), and it is even more highly correlated with PC1 (correlation coefficient is 0.93) than any individual indices alone. This significant correlation is a manifestation of the joint modulations that ENSO and NAO conditions have on EOF1. More explicitly, during concurrent El Niño and negative NAO

years, AR occurrence displaces equatorward; on the other hand, coexisting La Niña and positive NAO conditions tend to shift ARs poleward. These two scenarios are hereafter referred to as 'negative combinations' of ENSO and NAO. To further demonstrate the modulation of the negative combinations, we add the regressed SLP, IWV and wind fields against NAOI multiplied by -1 (hereafter -NAOI) to those against Niño 3.4 respectively. The sum of the regressed SLP against -NAOI (Figure 2.3a, shaded) and that against the Niño 3.4 index (Figure 2.3a, black contours) is presented as shading in Figure 2.3b. Due to the negatively superimposed ENSO condition, the NAO-like dipole has centers of action shifted westward relative to the canonical NAO pattern, and it is in accord with the SLP regressed onto AR PC1 (Figure 2.3b, black contours). They have a spatial correlation coefficient of 0.97. In a similar manner, to understand the roles of the negative combinations of ENSO and NAO in modulating thermodynamic and dynamic factors, an analogous procedure was done for IWV and the 850 hPa wind field. The sum of the regressed IWV onto -NAOI (Figure 2.3c, shaded) and Niño 3.4 index (Figure 2.3c, black contours) is displayed (Figure 2.3d, shaded). Also superimposed is the regression of IWV against AR PC1 (Figure 2.3d, black contours). They coincide extremely well with a spatial correlation coefficient close to 1. As can be seen in Figure 2.3, IWV contributing to AR PC1 is largely governed by ENSO, with a focused influence on west of the research domain. Regressed wind fields onto -NAOI, Niño 3.4 and their sum are shown in Figure 2.3e-g, respectively. The sum has a spatial correlation coefficient of 0.98 with the wind field regressed onto AR PC1 (Figure 2.2d). These pronounced spatial correlations provide further evidence that AR EOF1 is a result of the negative combinations of ENSO and NAO.

In conclusion, the southern lobe of the negative NAO dipole structure is a low-pressure center located just off the east coast of North America, and it shifts westerly belts equatorward during the

positive phase of EOF1 (Figure 2.3g, 2.2d). Together with enhanced IWV governed by El Niño conditions in the subtropics, they shift ARs equatorward; during negative phase of EOF1, however, ARs are displaced poleward due to the poleward-shifted westerly belts and suppressed IWV within 20-30°N latitude band during La Niña.

EOF2 in ensemble mean (a meridional concentration and dispersion)

EOF2 is a tripole pattern characterized by a meridional concentration or dispersion of AR frequency distribution and it accounts for 9.6% of the total variability (Figure 2.4a). During positive PC2 (black line in Figure 2.4b), AR occurrence is more concentrated within the 30-40°N latitude band, while it tends to dispersed to a northern band centered around 50°N and a southern band extending along 22°N during negative PC2. TNI is inversely correlated with PC2 and can explain nearly 40% of its total variability (Figure 2.4b and Table 2.1). SCAND index is also highly correlated with PC2 (r=0.54). In the map of correlation coefficients between PC2 and SST, marked correlations at 99% significance level are found in the central and easternmost tropical Pacific but with opposite signs (Figure 2.4e, shaded). This SST difference likely excites a wave train pattern which propagates and well projects onto a cyclonic circulation anomaly over the Labrador Sea (Figure 2.4e, black contours). This cyclonic anomaly is a part of the SCAND pattern. The regression of IWV onto PC2 is characterized by a tripole pattern with largest loadings in the west (Figure 2.4c, shaded). Significant values at 99% level are dotted. In wind field regressed onto AR PC2, only the significant values at 99% level are shown (Figure 2.4d). Strong westerly anomalies dominate the increase in AR occurrence over the 30-40°N band in AR EOF2.

EOF3 in ensemble mean (an increasing trend over Europe)

EOF3 is characterized by anomalies of one sign over northwestern Europe and the GOM, and weaker anomalies of the opposite sign in the vicinity of western Greenland and offshore northwestern Africa (Figure 2.5a). The positive phase of EOF3 features an elongation relative to the climatological distribution of AR occurrence in a southwest-northeast direction; the negative phase is characterized by a retraction. More explicitly, during positive PC3 (black line in Figure 2.5a), the GOM and European countries, especially Britain, are impacted by more ARs than normal years; during the negative phase, in contrast, the distribution of AR activities retracts and fewer ARs will arrive in Europe. This extension and retraction of AR occurrence at a basin scale accounts for 8.82% of the total explained variability.

In a manner similar to EOF1, IWV and wind fields are regressed onto AR PC3 to identify their respective contributions (Figure 2.5c&d). The interannual variability in AR occurrence over Europe and northwestern Africa is dominated by the dynamic factor, while the thermodynamic factor only exerts negligible influence over the western subtropical NA. During positive PC3, there is an anticyclonic wind anomaly over the Europe-North Africa sector, which results from the anomalous blocking high at sea level, as revealed in Figure 2.5e (black contours). Westerlies within the 50-60°N latitude band are strengthened, carrying large amounts of water vapor impacting Britain, Norway, and other northern European countries. In the meantime, easterly anomalies over the Iberian Peninsula and northeastern Africa dampen the IVT there. The regression field of IWV has only small amplitudes over Europe and northwestern Africa, and thus contributes little to anomalous IVT. Over subtropical western NA and west of the GOM, however, IWV varies with higher amplitude, but the variability in wind there is trivial. Consequently, IVT and hence AR occurrence barely varies from year to year over Cuba, Dominica and Puerto Rico.

Only weak IVT anomalies appear over the western GOM, carrying water vapor originating from tropical east Pacific northeastward into Mexico.

Interestingly, there is a long-term upward trend in PC3 and it is significant at the 99% level according to a Mann-Kendall trend significance test, suggesting that more ARs occurred over European countries during winters from 1951-2011. To explain this, PC3 was correlated with large-scale climate indices. It correlates with NAO, SCAND, and Niño 3 indices with linear correlation coefficients of 0.69, -0.46, and 0.38, respectively, all of which are statistically significant at the 99% significance level (Table 2.1). When correlating AR PC3 with global SST, Indo-west Pacific is a domain aside from Niño 3 region that has prominent correlation and they remain tightly connected even after removing their respective linear trends (not shown). This in part suggests that the interannual variability of EOF3 also comes from Indian and west Pacific Ocean, and a portion of the increasing AR occurrence over Britain may associate with the Indo-west Pacific SST warming since 1970s. It has been suggested and demonstrated that an observed strengthening of positive NAO is a result of the Indian Ocean warming (Hoerling et al. 2001; Sanchezgomez et al. 2008; Chu et al. 2017). Indeed, in the current study, differences in Z500, Z200, fields of air vertical motion and precipitation between the warm episode (1981-2011) and cold episode (1951-1980) of Indian Ocean agree well with those of Chu et al. (2017) (Figure S2.1 a-d), suggesting that by exciting wave trains via the released heat from anomalous tropical convections, Indian Ocean warming projects onto a positive NAO-like pattern over NA. In addition, after subtracting the regression coefficient of Indian Ocean area-averaged SST from original AR occurrence, a new AR occurrence matrix without the effect of Indian Ocean is obtained, after which an EOF analysis is performed. The original EOF3 or any similar counterpart characterizing a significant upward trend in AR frequency over northwestern Europe is missing

from the leading modes of EOF after the removal or in natural run. This trend again emphasizes that the enhancing AR occurrence over Europe is related to a strengthening positive NAO, which is in turn linked to Indian Ocean SST warming.

Contour lines in Figure 2.5e show the correlation coefficients between AR PC3 and global SLP, which is characterized by a dipole pattern reminiscent of a positive-phase NAO but with an eastward shift in the centers of action. As compared to the case in EOF1, this eastward shift in NAO structure is found to be caused by a positively superimposed ENSO effect. To explain this pattern, a new index is generated for EOF3, as has been done for EOF1, by adding normalized Niño 3.4 and NAOI. Its correlation coefficient with AR PC3 is 0.83 (Figure 2.5b), which is higher than the correlation between AR PC2 and any beforementioned individual indices. Comparable to the 'negative combinations' as detailed previously in EOF1, EOF3 is modulated by 'positive combinations' of ENSO and NAO effects, which includes coexisting +ENSO & +NAO / -ENSO & -NAO scenarios. In short, during concurrent positive ENSO and NAO conditions, more ARs affect northern Europe; when both ENSO and NAO are in their negative phase, ARs are more confined to the east coast of America and extratropical western NA. The sum of the maps of regression coefficients of SLP onto Niño 3.4 and NAO indices is an eastward shifted NAO-like pattern (Figure 2.6a, shaded). It bears considerable similarity to the regressed SLP field onto AR PC3 (spatial correlation coefficient is 0.97), with low pressure anomaly north of 60°N and a blocking high anomaly centered to the west of Azores (Figure 2.6a, black contours). In regressed IWV and wind fields, the effects of NAO are opposite to those of ENSO over most of the research domain. ENSO to a large degree decides the anomalous IWV field over western subtropical NA, and NAO contributes to the slightly positive IWV anomaly over Europe. The sum of regressed IWV fields (Figure 2.6b, shaded) highly overlaps with the regressed IWV field onto AR PC3

(Figure 2.6b, black contours), and they have a spatial correlation coefficient of 0.91. In the sum of regressed wind fields, most of the wind variability over the east coast of the U.S. and the subtropical NA associated with ENSO and NAO effects cancel out, but the anticyclonic anomaly over the Atlantic margin of Europe (Figure 2.6c, vectors), indicative of the blocking high as contoured in Figure 2.5e, still remains. The two wind field maps have a spatial correlation coefficient of 0.91. This evidence highlights the point that AR EOF3 is indeed a positively combined effect of ENSO and NAO.

AR-induced precipitation

To assess the impact of ARs over the NA, the relationship between DJFM AR events and precipitation is also examined. Here, AR-induced precipitation is estimated as the amount of precipitation with a concurrent AR event at each grid point (Figure 2.7a). Using the ratio of AR-induced precipitation to total precipitation, we find that overall, 60% of precipitation is associated with ARs over the entire east coast of North America (Figure 2.7b). ARs are responsible for 30-40% of the precipitation in Britain and northwestern Africa, and ~50% along the west coast of Iberian Peninsula. Moreover, ARs contribute notably to extreme precipitation events, identified using the ratio of AR-induced to total extreme precipitation (Figure 2.7c). Extreme precipitation is defined here as the precipitation exceeding 98th percentile at each grid point. The percentage reaches as high as 80% over subtropical NA and eastern U.S. Overall, ARs account for even higher percentages of the extreme rather than climatological rainfalls especially along coastlines such as the west coasts of Iberian Peninsula and northwestern European countries.

To characterize the contributions of modes of AR occurrence to precipitation, the AR-induced precipitation was regressed onto AR PC1 to PC3 (Figure 2.8a-c). The patterns of precipitation are

generally in line with the patterns of AR occurrence, which again demonstrates the robust relationship between AR occurrence and rainfall. The precipitation over the northern branch is more confined to the inland side because of the influence of Appalachian Mountains, which extends southwestward from Canada to Alabama (Figure 2.8a). Thus, ARs have focused impacts on the windward of the mountain chain, enhancing precipitation in places such as east of Tennessee during positive AR PC1. On the other hand, the lee side of the mountains such as in western North Carolina only receive lighter precipitation. The same holds true for the precipitation pattern related to EOF2 (Figure 2.8b). For EOF3, AR-induced precipitation has two maxima. One is over central NA and the other one is along the coast of northern Europe, near Scotland and Norway, due to orographic uplifting there (Figure 2.8c).

Internal variability

To improve NA AR prediction, understanding where its variability comes from is a prerequisite. Total variability consists of two independent components: forced variability and internal variability. Forced variability is the variability driven by external boundary forcing (e.g., prescribed SST and sea ice extent). It has a higher degree of predictability and is often referred to as the signal. Internal variability, however, is generated from nonlinear stochastic dynamics and usually hard to predict. To help reduce noise level and extract the forced part of the variability, we used a 30-member ensemble size. The average of the standard deviations of AR occurrence in 30 members at each grid point is used to represent the total variability. The standard deviation of the ensemble mean AR occurrence at each grid point is approximated as the forced variability. Next, we estimated the internal variability by taking a multiyear average of the standard deviations across the departures about the ensemble mean in 30 individual members.

The total variability is strongest over eastern NA along 30-35°N and a secondary maximum is located over southeastern U.S. (Figure 2.9a). Internal variability has a distribution similar to the total variability but with smaller amplitude (Figure 2.9c), especially over a band from the GOM to central NA, where forced variability dominates (Figure 2.9b). Note that the color scale for forced variability is only half of that for total variability. Considering internal variability as the noise and forced variability as the signal yields a map of signal-to-noise ratio (SNR) in DJFM AR occurrence over NA (Figure 2.9d.) Any value approaching or bigger than 1 means there is larger signal compared to noise, and AR occurrence in winter has higher potential predictability at the specific location. For example, most of Mexico, the southern part of Florida, Cuba, Dominica, and Puerto Rico all have SNR close to or larger than 1. In addition, a secondary peak extends from the central U.S. to southeastern Canada. The locations of the primary and secondary maxima in SNR coincide with the centers of action of the dipole pattern in AR EOF1 (Figure 2.2b). The area average AR count of the ensemble mean for both primary and secondary maxima are strongly correlated with those of JRA-55 (0.80 for the primary maximum and 0.44 for the secondary maximum). Both of these two domain-averaged AR counts are strongly controlled by ENSO, as indicated in EOF1, which explains why they have prominent SNR values.

An SNR analysis is also conducted for IWV and u850 fields (Figure 10e&f). Area-averaged westerlies and IWV over GOM are both highly correlated with Niño 3.4 and have strong forced variability. Over central U.S. to southeastern Canada, westerlies and IWV are inversely linked to Niño 3.4 index. The land effect of the U.S. continent likely decreases the stability and homogeneity in IWV and westerly appears to be more predictable than IWV. Their product, namely IVT, has reduced but still statistically significant SNR. Generally, ARs have higher degree of predictability over western NA, where ENSO's influences can still reach. Over Europe and northern Africa,

however, wind circulation over eastern NA is primarily modulated by NAO. The internal variability of simulated NAO, which is indicated by the range of variations in individual members, is quite big and dependent on the choice of member (not shown). The correlation coefficients between the NAO indices calculated from individual members and that from ensemble mean are low. Strong internal variability thus overcomes signal, lowering the potential predictability in ARs over Europe and northern Africa.

Conclusion and discussion

Summary

To unravel the interannual variability of the DJFM AR occurrence over NA-European (NAE) sector, large-ensemble simulations with a high resolution AGCM is employed in the present study. The climatology of AR occurrence in ensemble mean is capable of reproducing the mean state of reanalysis data, and a standard EOF analysis is then performed to the ensemble mean AR occurrence. The three leading modes of EOF explain 80% of the total variability. Several large-scale climatic factors including ENSO, PNA, NAO and SCAND and their linear superpositions are demonstrated to govern NA AR variability in the ensemble mean. The main characteristics of the three leading modes and their links to climate indices are summarized as follows:

1) EOF1 is a north-south dipole pattern modulated by 'negative combinations' of ENSO and NAO. This relationship is consistent across all 30 individual members. EOF1 accounts for over 60% of the total explained variability. The dominant signal of ENSO in ensemble mean shifts the dipole pattern southwestward relative to that in JRA-55. Consistent with our findings, Knippertz and Wernli (2010) found a positive correlation between poleward water vapor

transport over Gulf Stream region and Niño 3.4 in winter, which they relate to 'Mexican connection' (proposed by Rasmusson and Mo 1993).

2) EOF2 is a tripole pattern characterized by a meridional concentration and dispersion of AR occurrence at basin scale and this variability is related to SCAND and ENSO. It explains nearly 10% of the total variability.
3) EOF3 is mainly an increasing decadal trend in AR occurrence off and across the coast of northwestern Europe. The interannual variability is modulated by 'positive combinations' of ENSO and NAO and the trend bears some relation to the temporal evolution of NAOI towards a more positive phase during recent decades, which is suggested linked to Indo-west Pacific SST warming. EOF3 explains about 9% of the total variability.

The internal variability associated with wintertime AR conditions is also investigated. In general, AR events over lower latitudes have higher SNR ratio than those over higher latitudes. ARs over GOM and east coast of America is forced by central-eastern tropical Pacific SST anomalies and hence has higher predictability. On the other hand, AR variability over Europe is modulated by NAO, which is mainly a variability internal to the atmosphere and therefore, AR frequency there has rather random evolution and is hard to predict.

Discussion and implication

In the current chapter, the most striking finding is that different indices dominate over different locations and they exhibit distinct effects when two of them reinforce or cancel out each other depending on their phases. In the ensemble mean, for instance, ENSO may shift the centers of action of NAO dipole structure eastward or westward depending on whether it is positively or

negatively superimposed. This brings about an arguable question – the teleconnection of ENSO to NAE sector. ENSO's effect on tropical and extratropical Pacific is well studied but its teleconnection to NA is still under debate due to nonlinearity, non-stationarity and interevent variations (Gouirand and Moron 2003; Greatbatch et al. 2004; Toniazzo and Scaife 2006). Though some denied the relationship between ENSO and NAO (e.g., Rogers 1984), a number of studies have discovered that during El Niño, there is a circulation anomaly over NA projecting onto a negative phase of NAO (Toniazzo and Scaife 2006; Brönnimann 2007 and references therein); during La Niña, there is a circulation anomaly projecting onto a positive NAO (Pozo-Vázquez et al. 2001; Wu and Hsieh, 2004). Currently, there are both tropospheric and stratospheric evidence documented in literatures whereby ENSO influences NA atmospheric circulation. The first pathway is the downstream propagation of disturbances through wave trains excited from the tropical Pacific (Cassou and Terray 2001). Higher probability is found associated with positive (negative) polarity of NAO when there is anticyclonic (cyclonic) Rossby wave breaking far upstream in the North Pacific (Strong and Magnusdottir 2008a&b). Another most recognized tropospheric track is a modification on Atlantic Hadley cell via anomalous Walker circulation and subsequently tropical Atlantic SST anomalies (Klein et al. 1999). The changes in Atlantic Hadley cell lags ENSO signal by 3-6 months. For current study, no imprints of tropical Atlantic SST anomalies were found because seasonality is not taken into consideration. The third pathway needs propagation of anomalies via the stratosphere (e.g., Bell et al. 2009). Though there is only weak linear correlation between ENSO and NAO (r=-0.26 in the ensemble mean; only marginally significant at 95% level according to Student's t test), a scatter plot of NAOI versus normalized Niño 3.4 index (see Figure S2.2) highlights that higher probability is associated with 'negative combinations' of ENSO and NAO, in agreement with Li and Lau (2012), which used a 2000-yr

integration of a global coupled climate model. However, contrary to other findings which proposed that there is nonlinearity in the SLP anomalies between El Niño and La Niña events (Bell et al. 2009; Pozo-Vázquez et al. 2001; Gouirand and Moron 2003; Wu and Hsieh 2004; Toniazzo and Scaife 2006), in the ensemble mean, the SLP anomalies during El Niño years are generally mirror opposite to those during La Niña years, and the composites of SLP anomalies during extrema of ENSO indices do not correspond to a canonical NAO pattern in the ensemble mean (Figure S2.3). There are several factors that could have resulted in this disparity between observations and simulations. Firstly, AMIP-type simulations are driven by prescribed SSTs and thus the atmosphere and the ocean are not coupled. However, mutual influences of atmosphere and ocean are crucial in forming low-level baroclinicity and largely determine storms development, especially over the extratropics, where atmosphere has substantial influences on local ocean. Also, stratosphere is not well resolved in most AMIP-type models, so the mechanism involved the activity of stratosphere whereby ENSO may modulate NAO cannot be well simulated. Thirdly, the effects of ENSO are exaggerated in AGCM, likely blocking the influences of other dynamic factors and causing a bias. Additionally, we only focus on the same season (DJFM), and the seasonality and intra-seasonality, which might be the sources of the nonlinearity and interevent variabilities of ENSO signals, need to be taken into consideration in future research.

Under climate change, variabilities in SST and the atmosphere tend to alter. Strengthening wintertime Azores high and Icelandic low forced by SST warming patterns, which project onto a positive phase of NAO, tend to increase AR frequency over Europe (Kamae et al. 2019). Besides, there is a tendency for ENSO and NAO to become more negatively correlated in the future (Müller and Roeckner 2006). With these, an alteration is expected to occur to the storminess, cyclogenesis and AR variabilities over NA. The teleconnections of various climate patterns and how they will

respond under climate change are worth examining to improve seasonal predictions of NA AR activities so as to avoid or mitigate socioeconomic loss.

	NAO	PNA	SCAND	Niño 3.4	Niño 3	Niño 4	TNI
PC1	-0.60**	0.91**	-0.58**	0.90**	0.84**	0.84**	-0.21
detrend	-0.61**	0.91**	-0.60**	0.91**	0.87**	0.85**	-0.19
PC2	0.07	-0.24	0.54**	-0.10	-0.22	0.19	-0.62**
detrend	0.10	-0.24	0.55**	-0.10	-0.23	0.18	-0.65**
PC3	0.69**	0.10	-0.46**	0.30*	0.38**	0.27*	0.19
detrend	0.63**	0.15	-0.46**	0.32*	0.37**	0.25*	0.12

Table 2.1 Correlation coefficients between PC1-PC3 and large-scale climate indices. Correlation coefficients between detrended time series are also provided. Significant values at 99% and 95% significance levels based on a t-test are marked by ** and *, respectively.

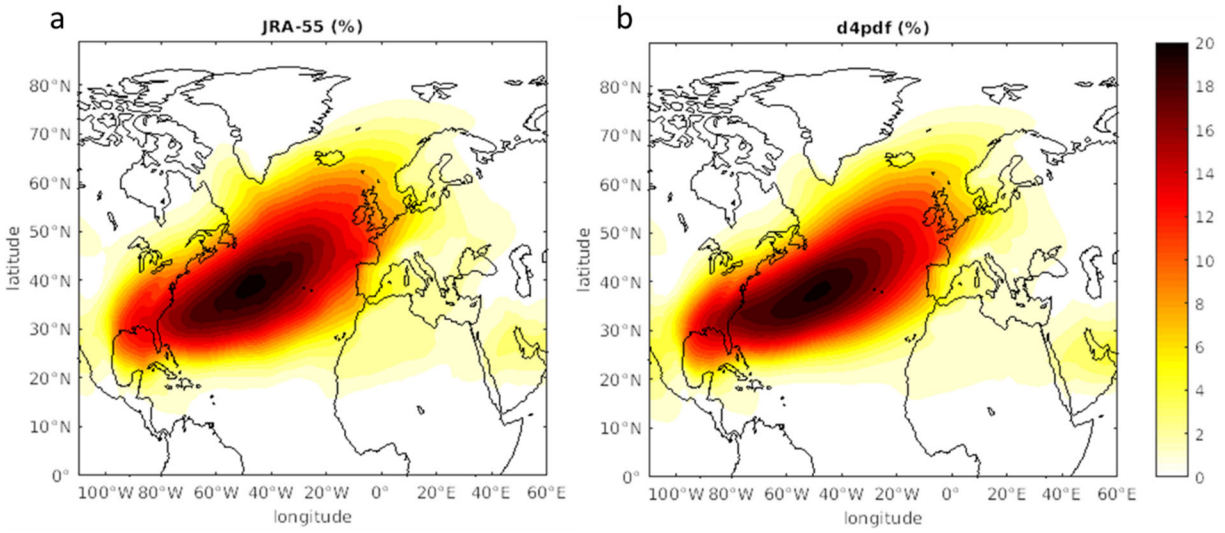

Figure 2.1 The climatology of DJFM AR occurrence. Climatology of AR occurrence (shaded, %) during 1958-2013 in (a) JRA-55, and during 1951-2011 in (b) 30-member ensemble mean. The occurrence at a specific grid point is calculated as the ratio of the number of 6-hourly time steps with an AR event to the total number of time steps.

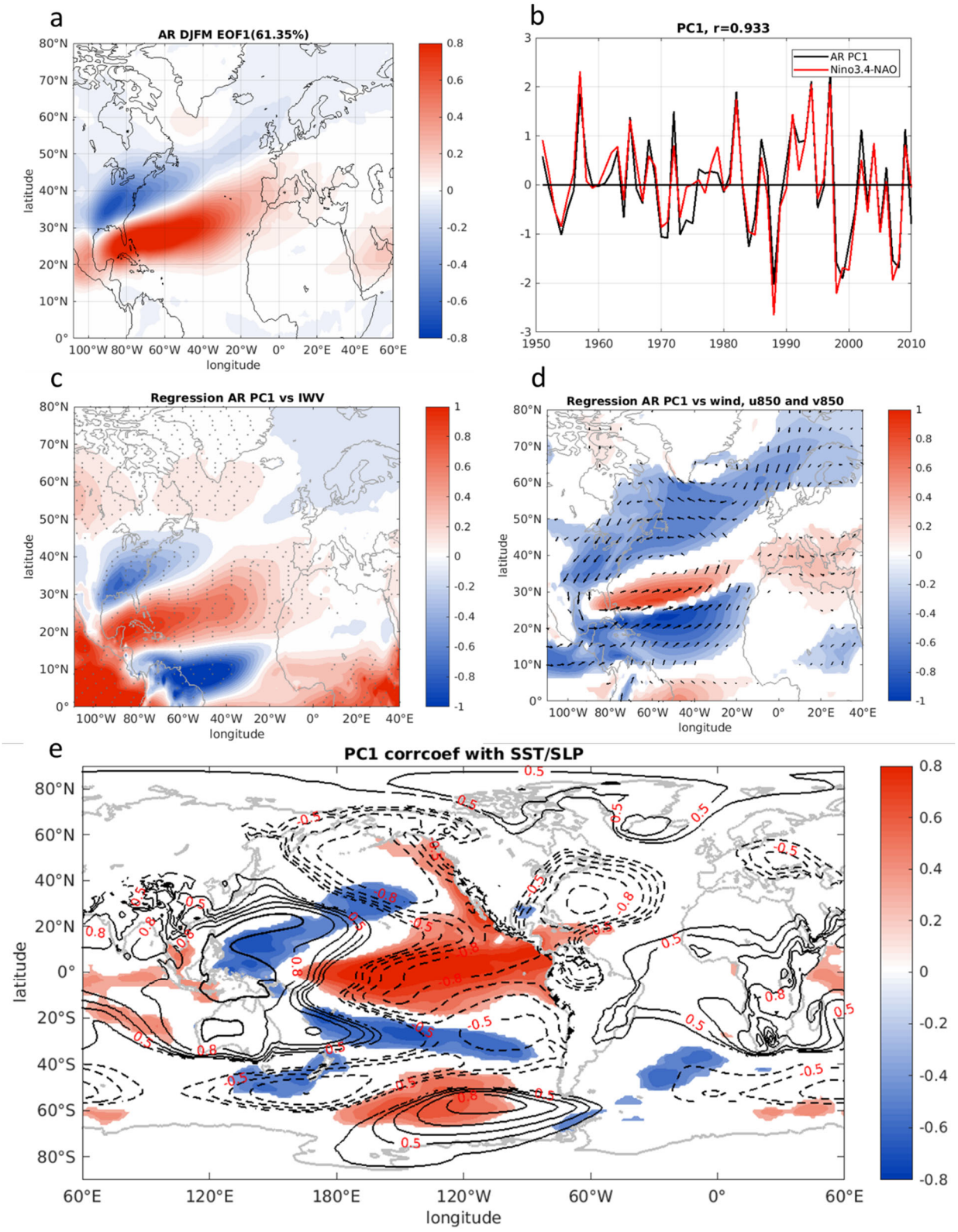
a
AR DJFM EOF1(61.35%)
latitude
longitude
b
PC1, r=0.933
AR PC1
Nino3.4-NAO
c
Regression AR PC1 vs IWV
latitude
longitude
d
Regression AR PC1 vs wind, u850 and v850
latitude
longitude
e
PC1 corrcoef with SST/SLP
latitude
longitude

Figure 2.2 EOF1 of DJFM AR occurrence frequency over the NA. (a) Spatial pattern of EOF1 (shaded), calculated as the seasonal mean AR occurrence anomalies relative to climatology. Color scale values are correspondent to unit standard deviation in PC1. (b) PC1 of AR occurrence (black, days/month) and a linear sum of normalized Niño 3.4 index and NAO index multiplied by -1 (-NAOI; red, unitless). The correlation coefficient between these two time series is 0.933, which is statistically significant at the 99% level. (c) Integrated water vapor (IWV) regressed onto PC1 (shaded, in kg/m2/s). Significant values at 99% level are stippled. (d) Wind magnitude (shaded, in m/s) and correspondent zonal and meridional winds (vectors, in m/s) regressed onto PC1. (e) Map of correlation coefficients between PC1 and global SST (shaded) and global SLP (contours), with negative contours dashed. Contour interval is 0.1. r=0.5 and r=0.8 are indicated. In (d) and (e) only significant values at 99% level are shown.

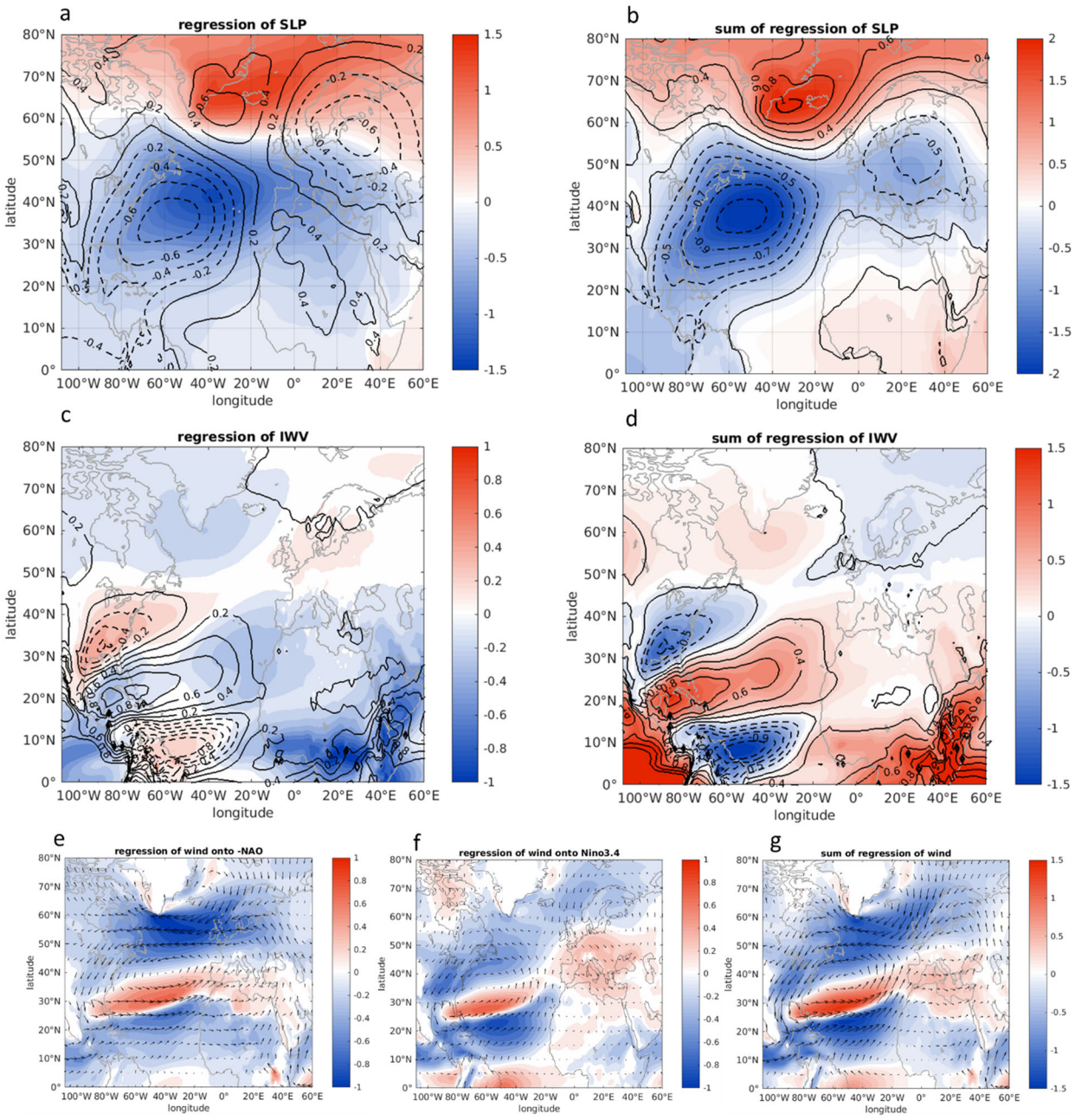
a
regression of SLP
b
sum of regression of SLP
c
regression of IWV
d
sum of regression of IWV
e
regression of wind onto -NAO
f
regression of wind onto Nino3.4
g
sum of regression of wind
latitude
longitude

Figure 2.3 The relationship between EOF1 and the 'negative combinations' of ENSO and NAO. (a) SLP regressed onto –NAOI (shaded, in hPa) and SLP regressed onto the standardized Niño 3.4 index (black contours, in hPa). (b) A sum of regression of SLP onto -NAOI and Niño 3.4 index (shaded, in hPa), and superimposed regression of SLP onto AR PC1 (black contours, in hPa). (c) As that in (a), but for regressed IWV field (shaded is for –NAOI, in kg/m3; black contours are for Niño 3.4, in kg/m3). (d) As that in (b), but for a sum of IWV regressed fields (shaded, in kg/m3), and superimposed IWV fields regressed onto AR PC1 for comparison (black contours, in kg/m3). Negative contours are dashed. Contour interval is 0.2. (e) Regressed wind magnitude (shaded, in m/s) and wind direction (vectors) onto -NAOI. (f) As that in (e), but for wind fields regressed onto Niño 3.4. (g) A sum of (e) and (f).

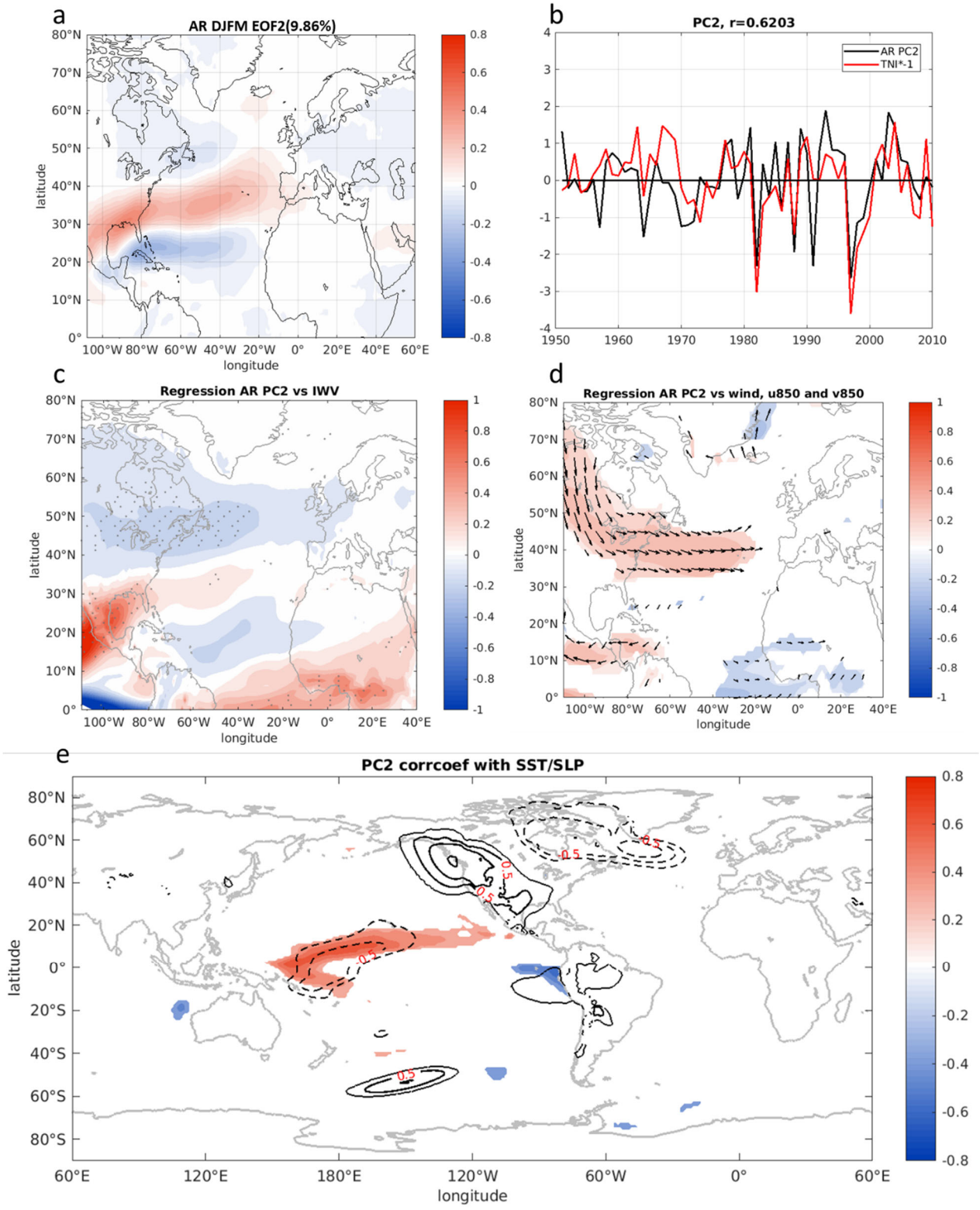
a
AR DJFM EOF2(9.86%)
latitude
longitude
b
PC2, r=0.6203
AR PC2
TNI*-1
c
Regression AR PC2 vs IWV
d
Regression AR PC2 vs wind, u850 and v850
e
PC2 corrcoef with SST/SLP

Figure 2.4 EOF2 of DJFM AR occurrence frequency over the NA. (a), (c)-(e) As those in Figure 2.2 but for EOF2. (b) PC2 of AR occurrence (black, days/month) and the TNI (red, unitless). The correlation coefficient between these two time series is 0.620, statistically significant at 99% level.

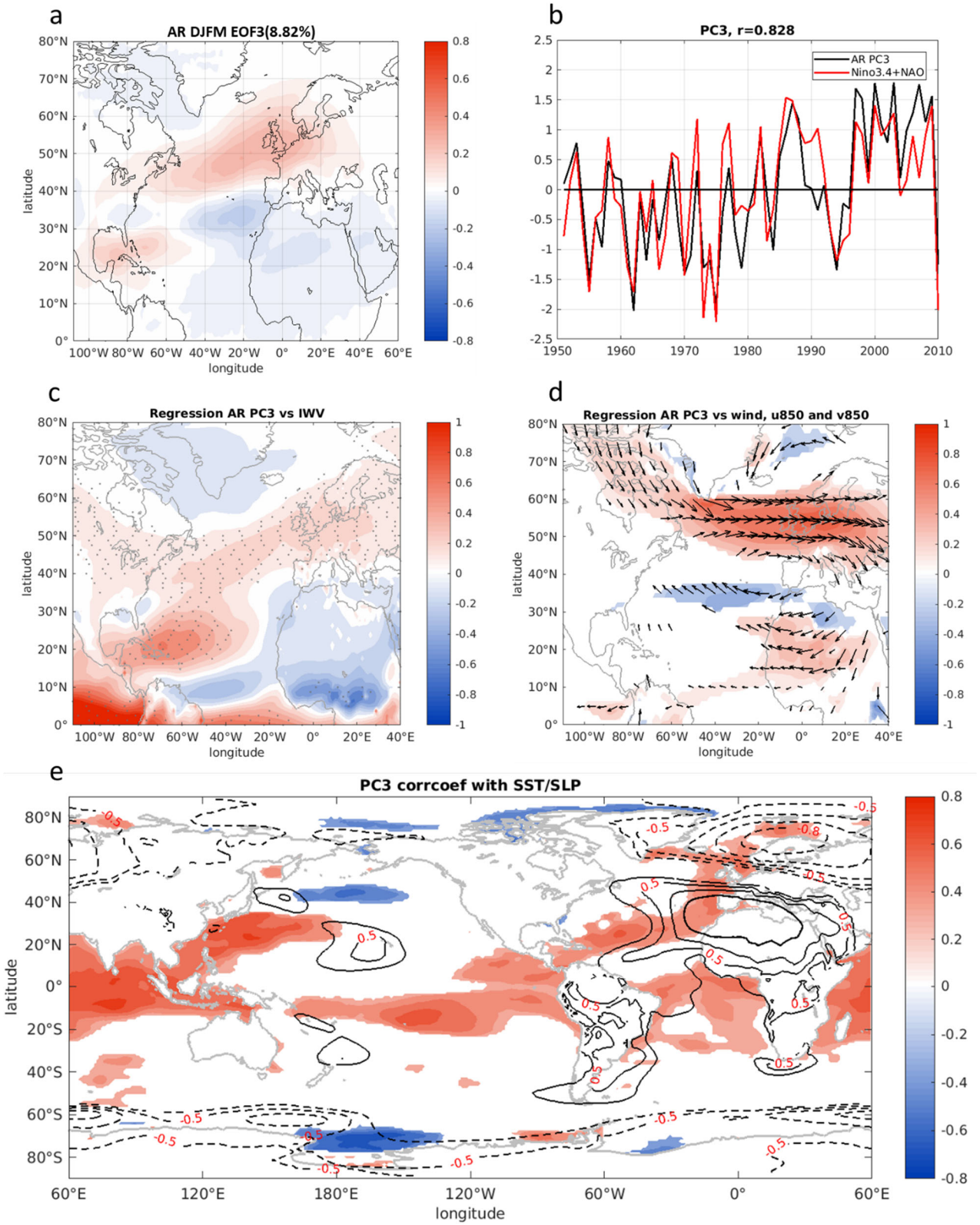
a
AR DJFM EOF3(8.82%)
latitude
longitude
b
PC3, r=0.828
AR PC3
Nino3.4+NAO
c
Regression AR PC3 vs IWV
latitude
longitude
d
Regression AR PC3 vs wind, u850 and v850
latitude
longitude
e
PC3 corrcoef with SST/SLP
latitude
longitude

Figure 2.5 EOF3 of DJFM AR occurrence frequency over the NA. (a), (c)-(e) As those in Figure 2.2 but for EOF3. (b) PC3 of AR occurrence (black line, days/month) and a standardized linear sum of Niño 3.4 index and NAOI (red line, unitless). The correlation coefficient between these two time series is 0.828, statistically significant at 99% level.

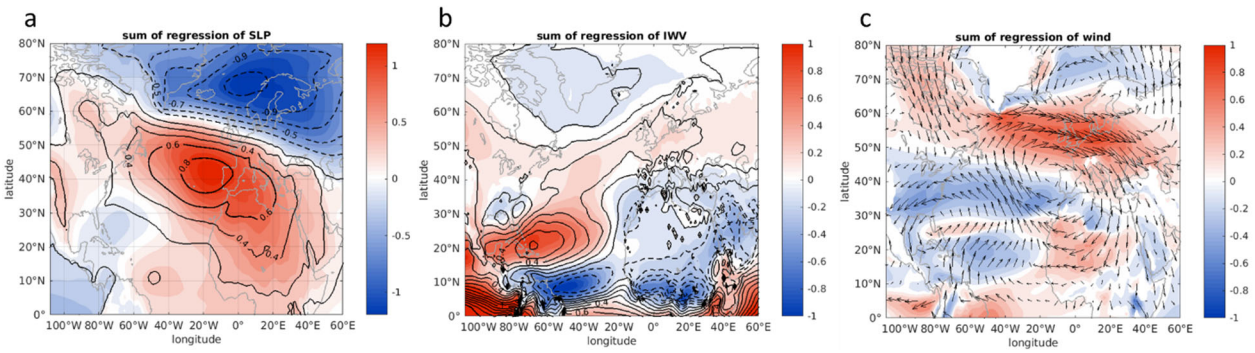

Figure 2.6 The relationship between AR EOF3 and the 'positive combinations' of ENSO and NAO. (a) A sum of regression of SLP onto NAOI and onto normalized Niño 4 indices (shaded, in hPa). Overlapped is regression of SLP onto AR PC3 (contours, in hPa). (b) As that in (a), but for a sum of regressed IWV field (shaded, in kg/m3). Superimposed is regression of IWV onto AR PC3 (contours, in kg/m3). Negative contours are dashed. Contour interval is 0.1. (c) As that in (a), but for a sum of regressed wind fields (shaded is for wind magnitude, in m/s; vectors are for u850 and v850).

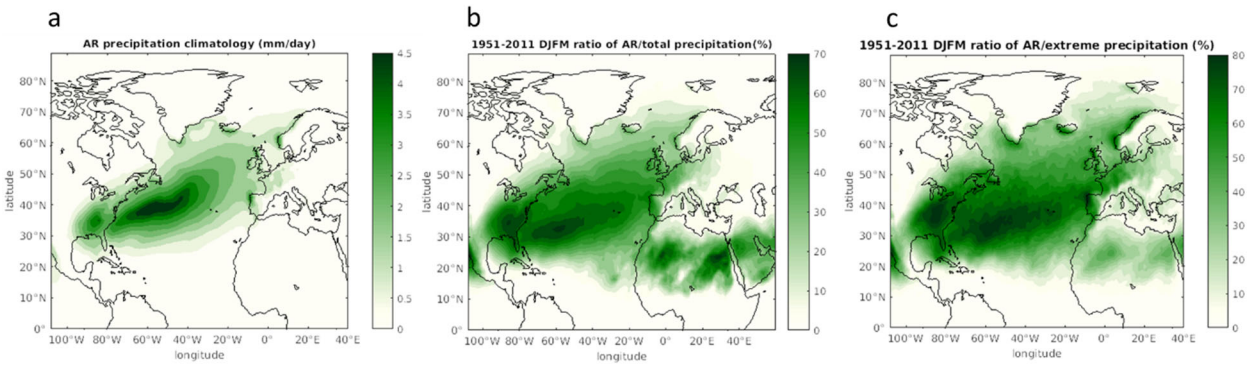

Figure 2.7 Precipitation induced by AR occurrence climatology in the ensemble mean. (a) DJFM AR-induced precipitation climatology during 1951-2010 in the ensemble mean (shaded, in mm/day). It is calculated as the precipitation with a concurrent AR event at each grid point. (b) Ratio of the sum of AR-induced precipitation to total precipitation (shaded, in %). (c) Percentage of the most extreme precipitation exceeding 98th percentile of the non-zero precipitation that is associated with ARs (shaded, in %).

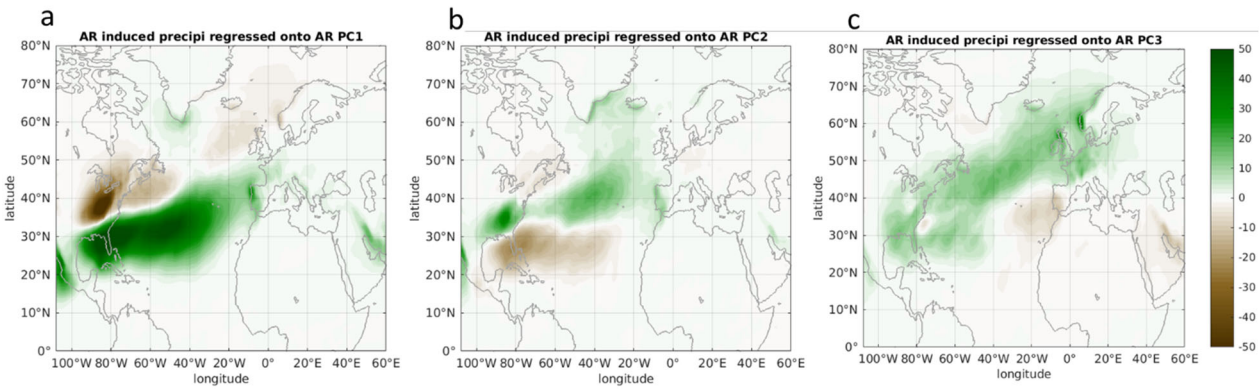

Figure 2.8 Precipitation induced by AR occurrence EOF1-EOF3. DJFM AR-induced precipitation regressed onto AR (a) PC1, (b) PC2, and (c) PC3 during 1951-2010 in the ensemble mean (shaded, in mm/day).

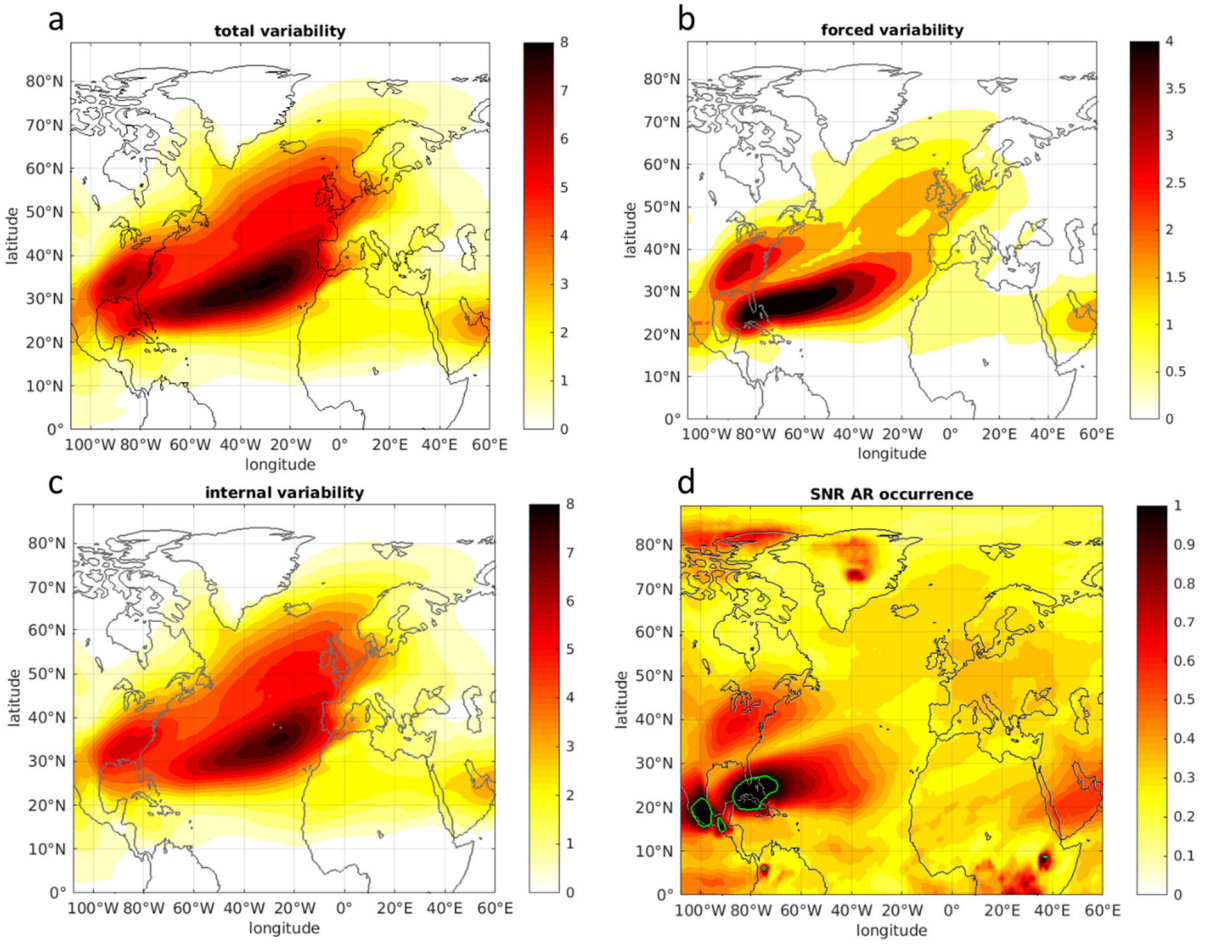

Figure 2.9 The predictability of DJFM AR occurrence. (a) Total variability in DJFM AR occurrence during 1951-2010 in the ensemble mean (shaded, in number). It is calculated as an average of the standard deviations of AR occurrence in 30 members at each grid point. (b) Forced variability is estimated to be the standard deviation of ensemble mean AR occurrence at each grid point (shaded, in number). (c) Internal variability is approximated as a multiyear average of the standard deviations across 30-member anomalies relative to the ensemble mean (shaded, in number). Note the smaller color scale for (b). (d) Signal to noise ratio (SNR), where forced variability is approximated as the signal while internal variability is regarded as noise (shaded, unitless). Contours of 1 are marked by green in (d).

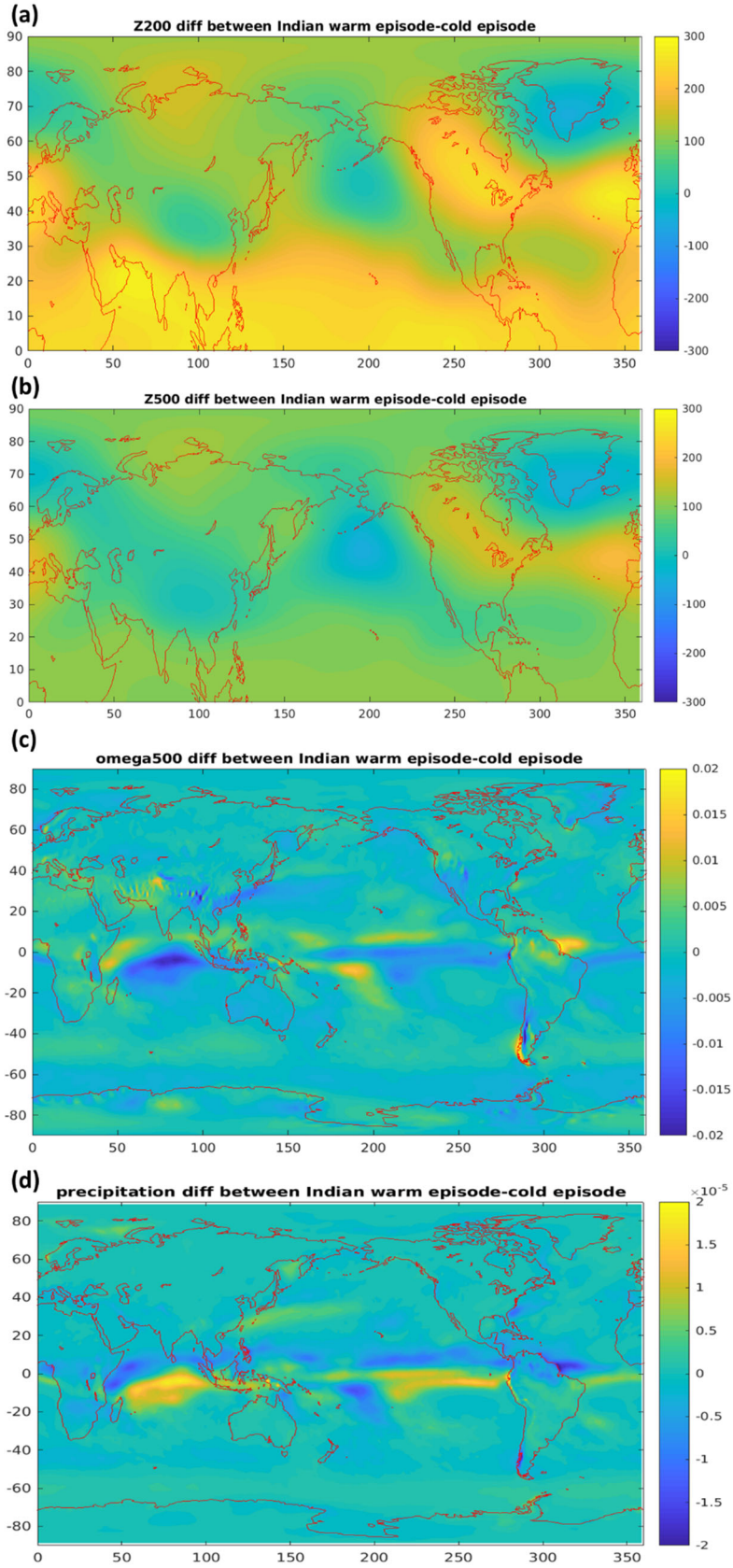
(a)
Z200 diff between Indian warm episode-cold episode
(b)
Z500 diff between Indian warm episode-cold episode
(c)
omega500 diff between Indian warm episode-cold episode
(d)
precipitation diff between Indian warm episode-cold episode
×10^-5

Figure S2.1 Differences in parameters between warm episode and cold episode of Indian Ocean SST. Differences in (a) Z500 (shaded, in m), (b) Z200 (shaded, in m), (c) subsidence flow at 500 hPa (shaded, in hPa/s) and (d) precipitation (shaded, in mm/day) between the warm episode (1981-2010) and cold episode (1951-1980) of Indian Ocean SST. Negative values in (c) indicate upward motion of air.

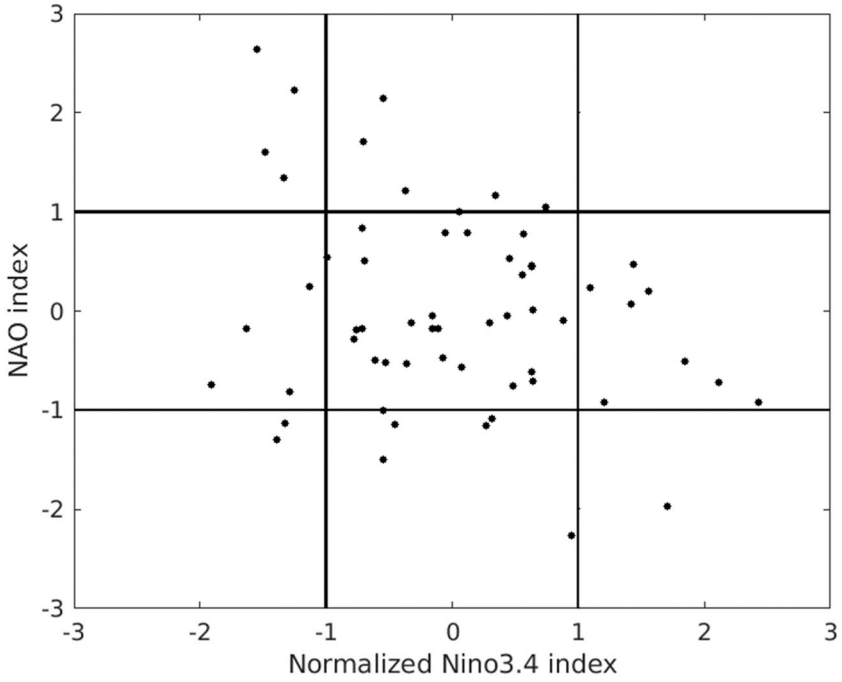

Figure S2.2 Scatter plot of NAO index versus normalized Niño 3.4 index in the ensemble mean.

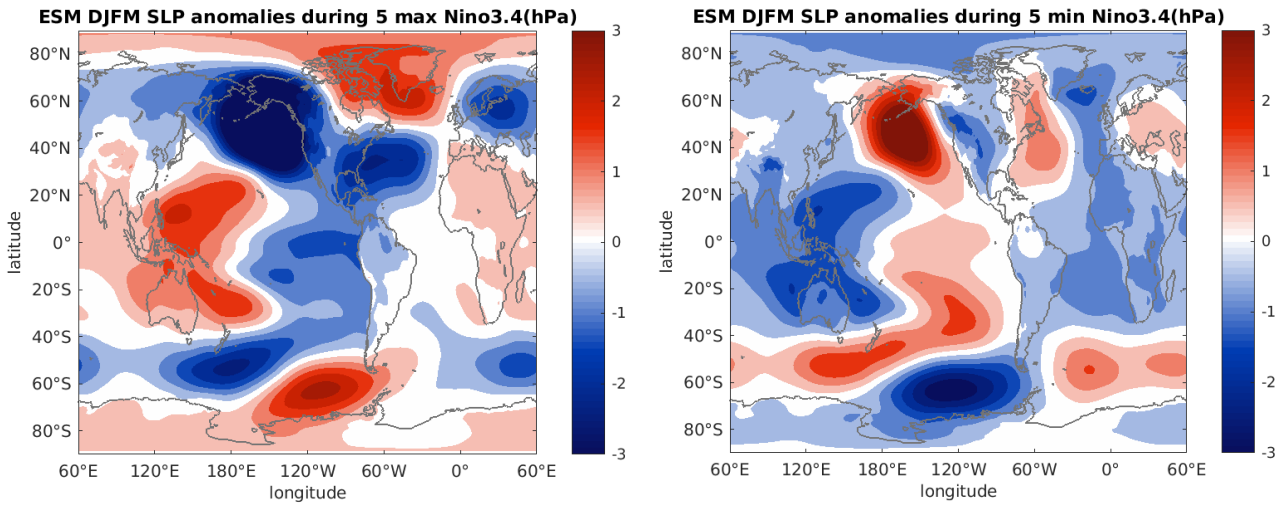

Figure S2.3 Composites of SLP anomalies during extrema of Niño 3.4 index. Composites of SLP anomalies during (Left) 5 maximum and (Right) 5 minimum Niño 3.4 index in ensemble mean (shaded, in hPa). Contour interval is 0.5 hPa.

CHAPTER 3: A CLUSTER ANALYSIS OF COLD-SEASON ATMOSPHERIC RIVER TRACKS OVER THE NORTH ATLANTIC AND LINKS TO EXTREME PRECIPITATION AND WINDS

Introduction

Atmospheric rivers (ARs), conduits of anomalous water vapor transport in the lower troposphere, are critical components in the hydrological cycles, in that they are responsible for over 90% of the poleward moisture flux in the global middle to high latitudes (Zhu and Newell, 1998). With this large amount of precipitable water carried along with them, ARs can cause extreme precipitation especially when encountering orographic uplifts (Ralph et al. 2006; Lavers et al. 2011, 2012; Leung and Qian 2009; Neiman et al. 2011; Bath et al. 2017); in addition, the low-level jets associated with ARs can cause severe wind damage (Waliser and Guan 2017). Communities that are impacted by ARs are thus more susceptible to precipitation- and strong wind- induced secondary disasters like flooding, landslides, storm surges, and coastal flooding (Ralph et al. 2006; Leung and Qian 2009; Neiman et al. 2008b, 2011; Waliser and Guan 2017; Khouakhi and Villarini 2016; Cordeira at al. 2019; Ridder et al. 2018). By generating landslides alone, ARs cause a loss of ~ 3.5 billion USD and 25-50 lives every year (Highland 2004). To minimize the huge socioeconomic repercussions brought by ARs, a more thorough understanding of the variability in their tracks and landfalling locations, and their impacts to particular regions, which will in turn help improve the predictive skills, cannot be overemphasized.

Community efforts like ARTMIP have been focused on evaluating and itercomparing AR identification/tracking algorithms (e.g., Rutz et al. 2019; Guan and Waliser 2019). The available

algorithms use a wide range of approaches (including differences in parameters, thresholds, etc.) to identify and/or track ARs (Figure 1 in Rutz et al. 2019). This diversity implies the challenges in using a unified approach to track ARs, and the most appropriate method should be dependent on the specific questions being addressed (Shields et al. 2018). Some other studies divided the AR events into distinct groups and examine their relationships with large-scale patterns of circulations. For example, Zhang and Villarini (2018) classified the ARs landfalling to west coast of U.S. into three clusters. They found that the Pacific-Japan pattern and the East Asian subtropical jet have strong links with two of the three clusters, and El Niño-Southern Oscillation (ENSO), Atlantic meridional mode (AMM), and the Pacific-North America (PNA) pattern drive the third cluster impacting the southwestern U.S. Tan et al. (2020) differentiated AR tracks over western North America into three subtypes using self-organizing maps and link different large-scale atmospheric circulation patterns with the subtypes. Kim et al. (2019) grouped the AR events over the northeast Pacific and western North America based on three phases of ENSO. They found central (eastern) Pacific El Niño favors ARs landfalling to western North America (southwestern U.S.), while fewer ARs can arrive at U.S. during La Niña conditions. As described above, though plenty of studies are focused on tracking or grouping ARs, limited work has been conducted to group AR trajectories.

In addition, while the abovementioned studies are focused on ARs over the U.S. west coast, only a few others investigate the landfalling ARs over the North Atlantic (NA) coastlines. For example, negative phase of North Atlantic Oscillation (NAO) favors landfalling ARs in the southern Europe (Eiras-Barca et al. 2016), whereas positive NAO is favorable for AR landfalls to the northern Europe (Lavers and Villarini 2013). East Atlantic pattern and Scandinavian pattern are also documented to have influences on AR occurrence in the Europe (Lavers et al. 2012;

Brands et al. 2017). Thus, an understanding about the heterogeneities of AR tracks and their impacts over the NA (especially the southeast U.S.) is still lacking, and this study is carried out to help fill the knowledge gap. Employing a curve clustering method, the AR tracks are divided into four main groups, each of which impacts a different geographical region of the NA. Section 2 presents the data and methods we use. The climatology of the total AR tracks identified in the simulation is compared and validated against the reanalysis dataset in section 3. The characteristics of the life-cycle of the four clusters, the underlying driving mechanisms, and their impacts to particular NA coastlines are then presented. A comparison between the simulation and the reanalysis is provided throughout section 3. Section 4 gives a conclusion and implications for future study.

Data and Methods

Reanalysis and simulations

In this study, we use both the Japanese 55-year reanalysis (JRA-55) and the first member (M01) of the ensemble simulations of Database for Policy Decision-making of Future climate change (d4PDF) to investigate the NA AR tracks. Here we only focus on the winter season from December 1st through March 31st (DJFM). JRA-55 covers a period from year 1958-2012, and M01 provides data from 1951-2010. M01 was performed with the 60-km-resolution Meteorological Research Institute atmospheric general circulation model (MRI-AGCM), version 3.2. More details about the model configuration and experiment setup can be found in Mizuta et al. (2017) and Kamae et al. (2017).

Following the detection algorithm in chapter 2, we use 6-hourly specific humidity and horizontal wind (zonal and meridional winds u&v) from 1000 hPa to 300 hPa to obtain the 6-

hourly AR occurrence and IVT datasets at 1.25° X 1.25° spatial resolution for AR tracking in both M01 and JRA-55. Sea surface temperature (SST) from the COBE SST at 1.0° X 1.0° for 1958-2013, SST from the COBE2 SST at 1.0° X 1.0° for 1951-2011, and sea level pressure (SLP) at 1.25° X 1.25° from JRA-55 and M01 are used to compare with the variations in AR tracks. The modes of large-scale climate variability and their indices used here including ENSO, PNA, and NAO are identical to those defined in chapter 2.

Tracking algorithm

The 6-hourly data can well resolve the movement of ARs considering that their travel speed can range from ~50 to 100 km/hr (Zhu and Newell 1994; Guan and Waliser 2019). In every 6-hourly snapshot, the IVT of an identified AR at each grid point is first spatially smoothed – an average of itself and its 8 neighboring grids is computed to replace the value at that point. The longitudinal and latitudinal positions of the 9-grid-smoothed maximum IVT versus time are then recorded for each AR detected in each snapshot. The tracking algorithm is based on the spatial proximity of the IVT maxima between two consecutive time steps – a distance threshold of 1200 km is used here to distinguish different AR events, and equatorward or westward movements from t to t+1 except small bounces are prohibited. A sensitivity test has proved that 1200 km is a reasonable threshold considering both the typical translation speed of ARs and the jump of the smoothed maximum IVT location. Of the total tracks identified, only those over the NA (110°W – 40°E, 0-90°N) and lasting longer than 8 time steps (i.e., 2 days) are retained, yielding 2033 tracks in M01 and 2226 tracks in JRA-55 for DJFM from 1958-2013. A sensitivity test on the choice of domain and minimum duration of the tracks reveals that the result is quite robust.

Cluster analysis

A curve clustering method developed by Gaffney et al. (2007) is employed here to group the AR tracks into four distinct clusters based on their genesis locations and geometric shape of the subsequent tracks. We tested three to nine as the number of clusters. Four clusters can best represent all of the shape types of AR tracks, and each of them can be well explained by the large-scale climate modes. The method is built upon a finite mixture model in which the data distribution is a convex linear combination of component density functions. Here we test several polynomial regression functions and finally choose to use the quadratic polynomial which can best model the longitude and latitude versus time of the tracks. Every track is assumed to be generated by one of the K (K=4 in this study) regression models, each of which has different shape parameters. After learning about the parameters of the all the K models associated with the AR tracks, each track is assigned to one of the K mixture components (i.e. clusters) that has the highest probability to have generated that track. A more detailed description of the clustering methodology is well documented in Camargo et al. (2007).

Results

Climatology of track density

In general, the DJFM total track density in M01 and JRA-55 both during the shared time interval 1958-2011 exhibit similar patterns of distribution (i.e. the southwest-northeast tilt of the orientation, highest track density over the eastern-central NA; Figure 3.1). There is a small underestimate (4% less in M01) of the total track number in the model, which is consistent with the tendency that most of the models underestimate the frequency and intensity of extratropical cyclones in the current climate (Seiler and Zwiers 2016b). The track density along the entire NA coastlines in M01 generally bears remarkable resemblance to that in JRA-55, which confirms that

M01 has the capability in capturing the large-scale features of the AR trajectories in the observations, and the same conclusion can be made using other reanalysis datasets. The results produced by different reanalysis datasets or individual members are consistent, and here we only present the results using JRA-55 and a representative member.

Characteristics of the four AR clusters

In this section, a cluster analysis is employed to group the AR tracks identified into four different clusters based on their geographic locations and geometric characteristics (see section Data and Method for details of the clustering method; Figure 3.2 a-d). The tracks and track density of the four clusters in the JRA-55 present strikingly similar pattern (Figure 3.2 e-h). The following description will be based on M01 for brevity. In M01, cluster 1 is characterized by a zonal distribution of the locations of AR genesis along the 20-40°N latitudinal band, and an initially zonal and then northward curved average track indicated by the green curve (Figure 3.2a). The Atlas Mountains in the northwestern corner of the African continent separate the AR tracks into two branches. The branch coming from the open ocean is directed northward by the topography to impact Iberian Peninsula, leaving a shadow of zero track density to the east of the Atlas Mountains. Another branch originates over inland Africa and curves northeastward to the Mediterranean Sea. The track density of cluster 1 is the lowest among the four clusters (only 271 tracks) with a rather zonal distribution and a maximum located off the Atlantic coast of southwestern Iberian Peninsula (Figure 3.2a).

Cluster 2 has the highest track number (747 tracks). The tracks have origins concentrated in the west of the research domain, about half of which originate from the eastern North America continent. The average track starts from just off the coast of North Carolina and then travels across

the basin to arrive at the U.K. (Figure 3.2b). The highest track density is off the east coast of North America at 40-45°N (Figure 3.2b).

Cluster 3 has 573 tracks that are overall shifted westward and equatorward compared to those in cluster 2 (the shift is more obvious between the green lines), and most of them originate over the mainland U.S. Some ARs generated from the easternmost North Pacific that have impacts on NA are also included (Figure 3.2c). The maximum track density appears over the eastern U.S. continent (Figure 3.2c).

The origins of the tracks in cluster 4 (701 tracks in total) scatter all over the high-latitude NA, and the subsequent tracks have footprints along the entire Atlantic margin of Europe and even penetrate into farther inland to affect Russia (Figure 3.2d). The average track is pointing from the central NA to the west coast of Norway. Though the maximum track density is over the open ocean, U.K. is heavily impacted by this cluster (Figure 3.2d).

Generally, IVT of the tracks is stronger above the ocean than on the land, especially over the western NA basin (Figure 3.3 a-d), where lies the warm pool. Warm SST increases the above-lying air temperature to increase the saturated vapor pressure, which in turn strengthens the water vapor content and hence IVT. For example, some weak ARs in cluster 2 and 3 generate from the continent but immediately get stronger when they travel above the warmer ocean (Figure 3.3 b&c). These ARs soon weaken and dissipate after they make landfall to the east coast of NA.

To examine the characteristics of the four clusters, the probability density functions (PDFs) of their lifetime maximum IVT, lifetime mean IVT, and duration are shown in Figure 3.4 a-c, respectively. Cluster 1 has a positive-skewed distribution in all of the three metrics– on average, the tracks in cluster 1 has the lowest intensity and shortest duration. Cluster 2 and 3 have very similar distribution in terms of the intensity, all climaxing at around 1300 (950) kg/(m·s) for

lifetime maximum intensity (lifetime mean intensity). Both have higher fractions of strong ARs. Cluster 4 has a distribution of intensity lying in between, peaking at about 1000 kg/(m·s) for lifetime maximum intensity and 800 kg/(m·s) for lifetime mean intensity. The PDFs of duration show that cluster 1 and 4 are rather short-lived clusters, peaking at about 60 hours. Cluster 2 and 3 have a flatter distribution extending towards the longer duration (Figure 3.4c). In general, tracks that originate from west of NA have higher intensity due to the warmer SST, and longer duration because of the longer travel distance, while tracks in cluster 2 and 4 quickly landfall and dissipate (Figures 3.3 & 3.4).

Associations to modes of large-scale climate variability

To examine the large-scale climate variability underlying the variations in the tracks, maps of correlation coefficients between global SST/SLP and the time series of the track numbers of each cluster are shown in Figure 3.5. The correlation map of cluster 1 is characterized by a negative phase of NAO-like dipolar structure in the SLP field over NA (black contours in Figure 3.5a). The correlation coefficient between NAO index and the track number in cluster 1 is -0.67 (Table 3.1), statistically significant at 99% level. A comparable table for JRA-55 is also presented (Table 3.2), which shows a very similar result as that in the M01. The track counts in cluster 2 are negatively correlated with the equatorial Pacific SST, while in cluster 3 they are in positive correlation (color shading in Figure 3.5 b & c). Also, a negative PNA-like wave train pattern in the SLP filed can be seen in Figure 3.5b, and over NA it projects onto a westward-shifted NAO-like pattern. In the map of cluster 3, the PNA signal is rather weak but a negative NAO-like pattern is obvious. The correlation table provides further evidence to support these relationships (Table 3.1). In other words, a combination of La Niña and positive NAO conditions favors AR tracks over the western

NA, and coexisting El Niño and negative NAO scenarios are favorable for tracks that impact North American east coast. In contrast to cluster 1, cluster 4 is associated with positive phase of NAO. In summary, positive NAO favors ARs striking northwestern Europe; negative NAO shifts AR tracks southward to impact Iberian Peninsula and northwestern Africa. The time series of the track count in the four clusters are plotted against the correspondent modulating climate indices (Figure S3.1).

Linkages to extreme precipitation and winds

ARs can cause extreme precipitation and strong winds (e.g., Waliser and Guan 2017), which are the two precursors for secondary disasters like flooding, landslides, storm surge, etc. Here, we investigate the percentage of the most extreme precipitation or wind speed (defined as those exceeding the 98^{th} percentile of nonzero values at each grid point) that coincides with the passage of an AR track for total AR tracks that last longer than two days (Figure 3.6) and also for each cluster separately (Figure 3.7). The extreme rainfall or wind speed is considered as AR-induced as long as it happens within one day after the passage of an AR track.

The overall AR tracks account for over 80% (70%) of the 98th percentile extreme precipitation (winds) along inland and the east coast of U.S. (Figure 3.6). West coast of Europe like Iberian Peninsula is severely affected by the strong wind associated with ARs – more than 70% of the wind extremes can be attributed to ARs. The percentage of extreme rainfall that is induced by ARs varies from 70% in the Iberian Peninsula to about 50% in Europe. Another maximum is over the central NA along the 30-40°N latitudinal band.

Next, the influence of each cluster on the rainfall and wind extremes is investigated. Cluster 1 contributes to around 25% of the extreme rainfall and wind speed over Iberian Peninsula (Figure

3.7 a&b). In addition, 25% of the extreme precipitation in the southeastward of Atlas Mountains is related to ARs in cluster 1. Tracks in cluster 2 have highest impact over the western NA (Figure 3.7 c&d). Their influence on the coastlines is quite marginal – only 10% of the extreme precipitation and wind along the U.S. east coast and European countries are related to cluster 2. Cluster 3 accounts for more than 50% (40%) of the extreme precipitation (winds) over east coast of North America and U.S. states including Tennessee, Kentucky, and Indiana (Figure 3.7 e&f). Cluster 4 can explain about 20% of the extreme precipitation over the U.K. and 30% along the west coast of Norway and southern Iceland, while cluster 4's wind impact is more focused on southern U.K., France, and Germany (Figure 3.7 g&h).

Conclusions and discussions

In this chapter, we investigated the categorization of the cold-season AR tracks and its linkages to the most extreme precipitation and winds over the NA. Based on a curve clustering method, the DJFM AR tracks over the NA were grouped into four different clusters, each of which impinge impacts on a different geographic region. The characteristics of the four clusters and their associations to large-scale climate variability are summarized as follows:

1. Cluster 1, with the lowest track density and weakest intensity, is governed by a negative polarity of NAO, making landfall to Iberian Peninsula, Mediterranean Sea, and northwestern Africa. It accounts for 25% of the most extreme precipitation and wind speed along the Atlantic margin of Iberian Peninsula.
2. Cluster 2 has the largest track number, and its highest track density is over the open ocean. Concurrent negative phase of PNA and La Niña conditions favor ARs generating from the west of the NA and making landfall to Europe. The long travel distance over the ocean enables the tracks in cluster 2 to live longer.

3. Cluster 3 displaces south- and westward compared to cluster 2 and impacts central-to-eastern U.S. during coexisting negative NAO and El Niño scenarios. The overall AR tracks account for over 80% (70%) of the extreme precipitation (winds) along the U.S. east coast, with largest contribution from cluster 3.
4. Cluster 4 is more short-lived, striking northwestern Europe most likely during the positive phase of NAO. Up to 25% of the extreme precipitation and winds along the Atlantic margin of the northern European countries are attributed to it.

In regards with the shape of the clusters, it is worth noting that clusters 2—4 all have a southwest-northeast orientation in their average tracks (green lines in Figure 3.2), which is consistent with the poleward deflection of storm tracks at the exit region of the jet (Hoskins et al. 1983; Orlanski 1998). Meanwhile, the general consistency in the shape of the tracks among the four clusters also indicates that the location of genesis is a much more important factor for the classification of clusters.

Among the four clusters, cluster 3 that represents the branch of ARs impacting the southeastern U.S. has profound implications. Though cluster 3 explains more than half of the most extreme rainfall there, it has not been well studied. The facts that cluster 3 is modulated by ENSO events, and ENSO could be well predicted at seasonal leads, indicate that cluster 3 must have some levels of predictability. As such, further work directed at the mechanisms underlying the relationships between ENSO phases and track number in cluster 3 would be a future direction. Indeed, more investigations into cluster 3 and its predictability using large-ensemble simulations could shed lights on the weather forecasting, policy-making, and water resources management for the communities in the southeastern U.S. Similarly, the predictability and its sources at subseasonal

to seasonal time scales associated with other clusters of NA AR tracks are also interesting topics to address.

Cluster	1	2	3	4
NAO	-0.67**	0.30*	-0.41**	0.69**
PNA	0.32*	-0.36**	0.30*	-0.41**
EA	-0.22	0.21	0.08	0.11
SCAND	-0.01	0.006	-0.16	0.06
Niño3.4	0.06	-0.41**	0.35**	-0.13
Niño3	0.07	-0.38**	0.37**	-0.06
Niño4	0.07	-0.36**	0.27*	-0.18

Table 3.1 Correlation coefficients between track counts and climate indices in M01. Correlation coefficients between annual time series of number of tracks in each cluster and large-scale climate indices in M01. Values that pass the 99% and 95% significance level are marked with ** and *, respectively.

Cluster	1	2	3	4
NAO	-0.83**	0.46**	-0.34**	0.64**
PNA	-0.10	-0.18	0.13	0.22
EA	-0.07	0.17	-0.23	-0.03
SCAND	0.04	0.30*	0.14	-0.08
Niño3.4	0.22	-0.35**	0.36**	-0.24
Niño3	0.17	-0.28*	0.33**	-0.14
Niño4	0.27*	-0.33**	0.32*	-0.35**

Table 3.2 Correlation coefficients between track counts and climate indices in JRA-55. Correlation coefficients between annual time series of number of tracks in each cluster and large-scale climate indices in JRA-55. Values that pass the 99% significance level are marked with **.

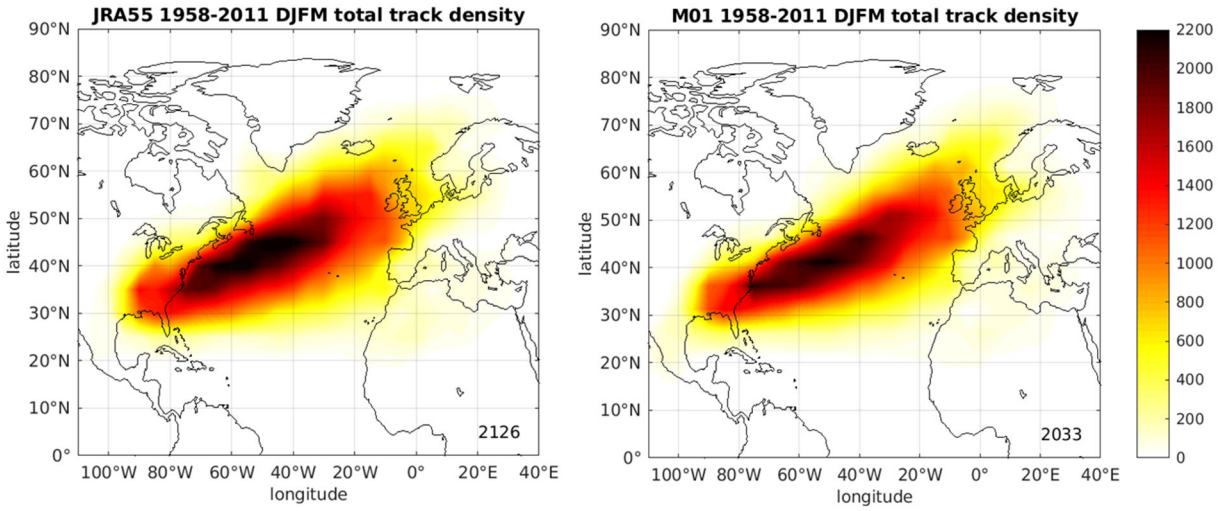

Figure 3.1 DJFM total AR track density over the NA during 1958-2011. The track density is binned into 5° x 5° grid box in (left) M01 and (right) JRA-55. Numbers in the right bottom corner in each graph indicate the number of the total tracks identified.

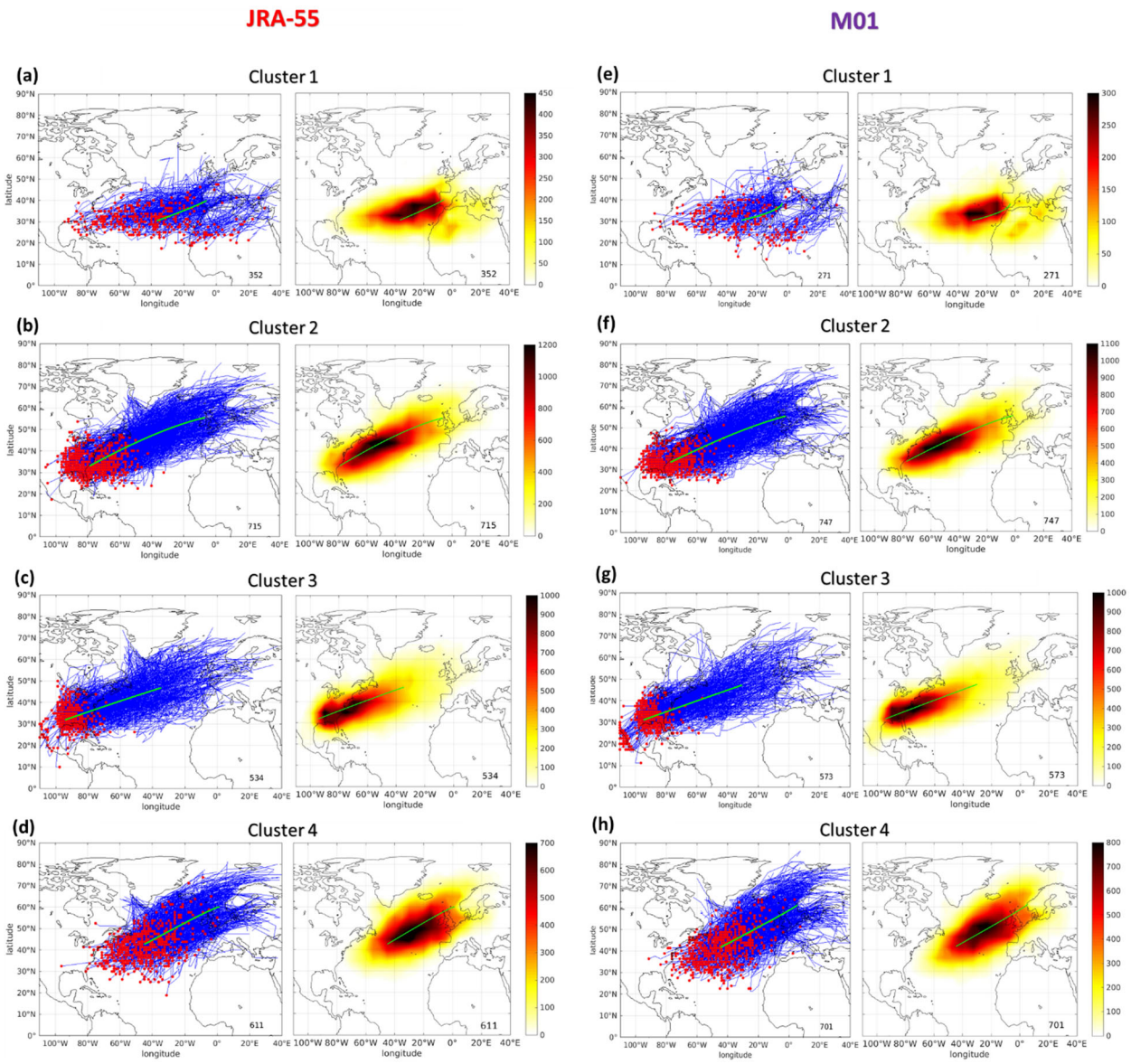

Figure 3.2 The four clusters of DJFM AR tracks according to a curve clustering method. (a)-(d) Left column: Origins (red dots) and subsequent tracks (blue lines) of cluster 1-4, respectively. An average of the tracks is shown in green curve for each cluster. (a)-(d) Right column: Track density of cluster 1- 4, respectively, which is calculated as the time an AR track passes a 5° x 5° grid box. Note that the scale bar is different for each cluster. (e)-(h) As those in (a)-(d), but for JRA-55.

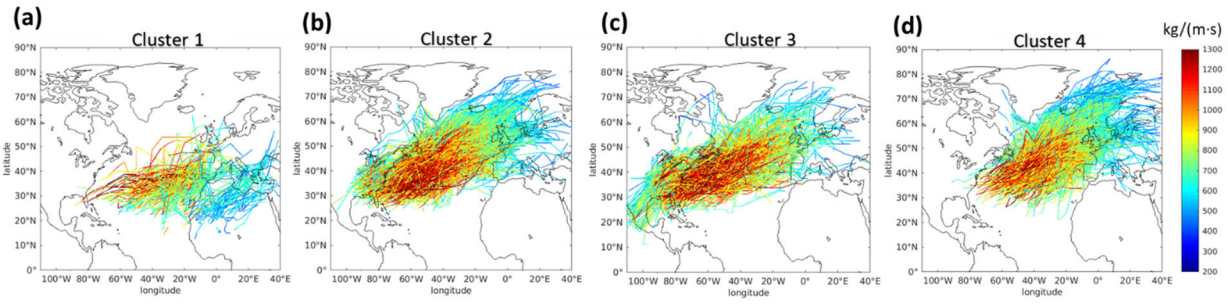

Figure 3.3 Tracks of four clusters as a function of AR intensity. Tracks of (a) cluster 1, (b) cluster 2, (c) cluster 3, (d) cluster 4 plotted as a function of IVT (color; in kg/m·s^{-1}).

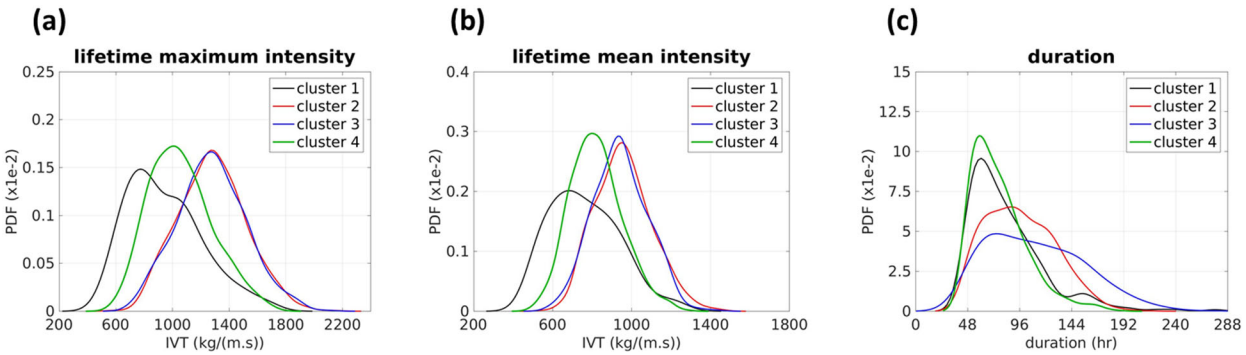

Figure 3.4 PDFs of lifecycle characteristics of the four clusters. PDFs of (a) lifetime maximum intensity, (b) lifetime mean intensity, (c) track duration in cluster 1-4.

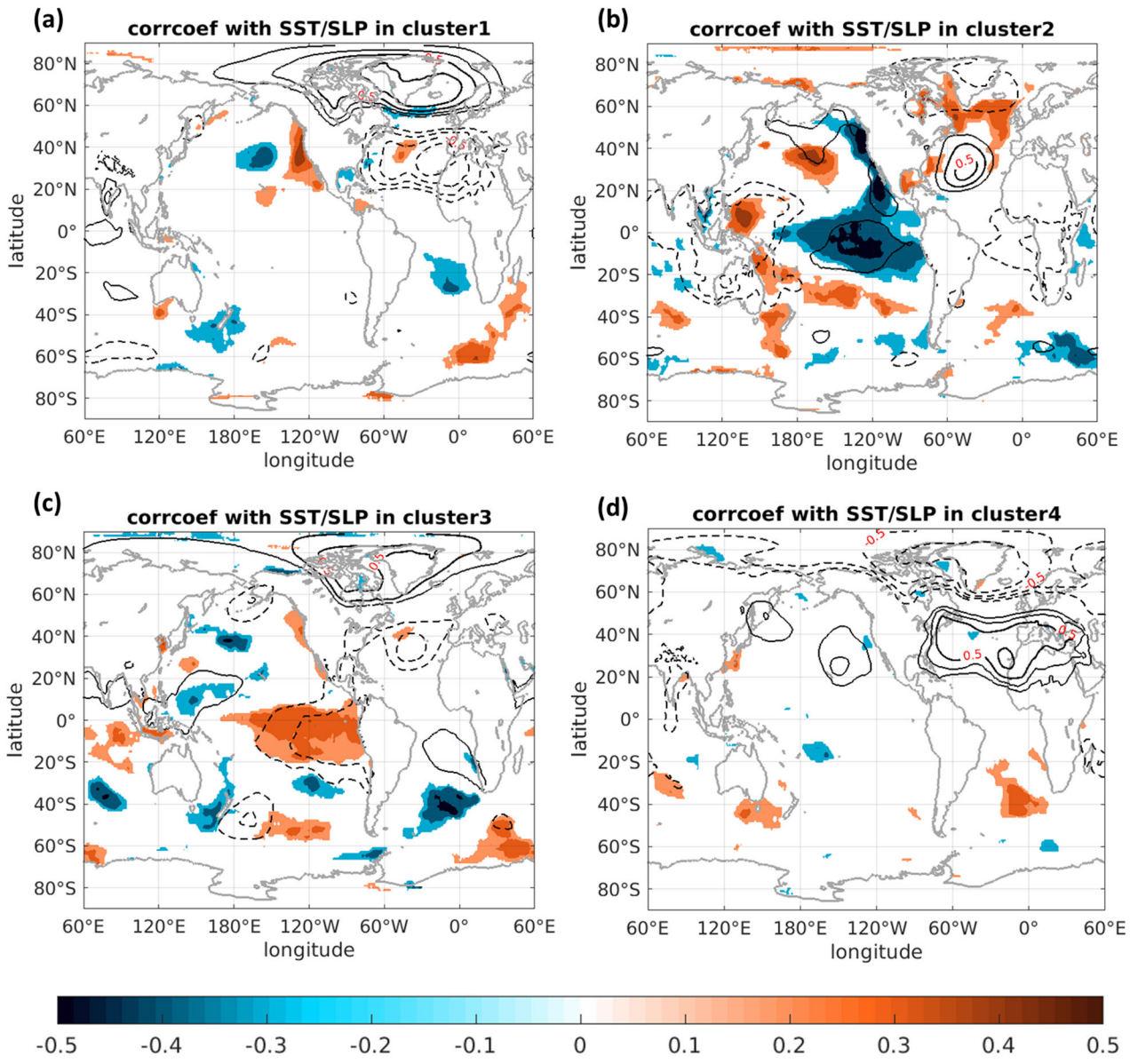

Figure 3.5 Map of correlation coefficients between SST/SLP and track number of the four clusters. SST (color shaded), SLP (black contours) and annual time series of track counts in (a) cluster 1, (b) cluster 2, (c) cluster 3 and (d) cluster 4. Contour interval is 0.1 for both the shading and the contour lines, and contours of value ±0.5 are marked.

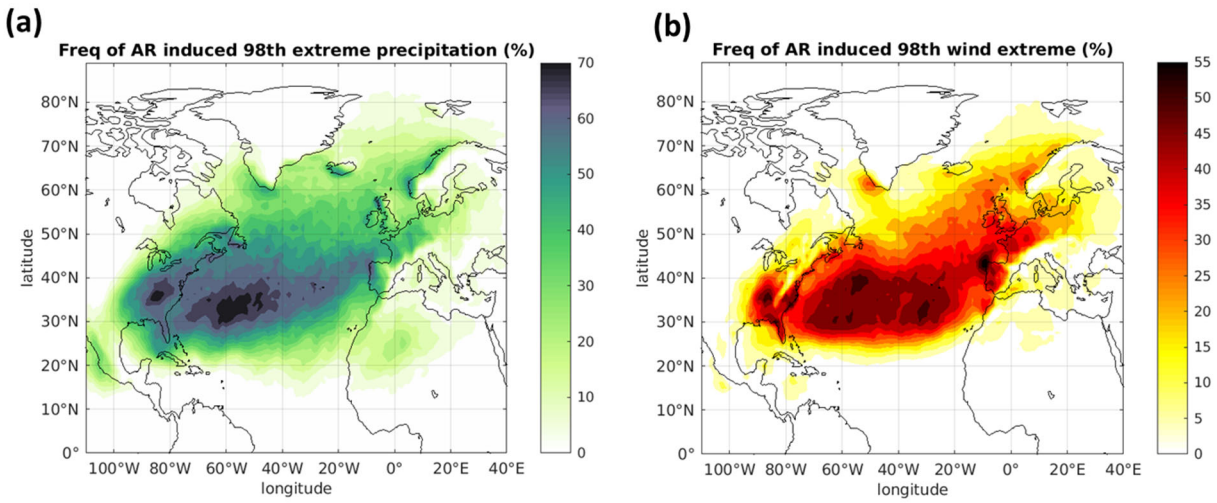

Figure 3.6 Frequency of extreme precipitation and winds induced by total AR tracks. Frequency of (a) extreme precipitation and (b) winds that is caused by identified AR tracks. The extreme precipitation and winds are defined as those exceed their respective 98th percentile of nonzero values at each grid point. The contour interval is 5%.

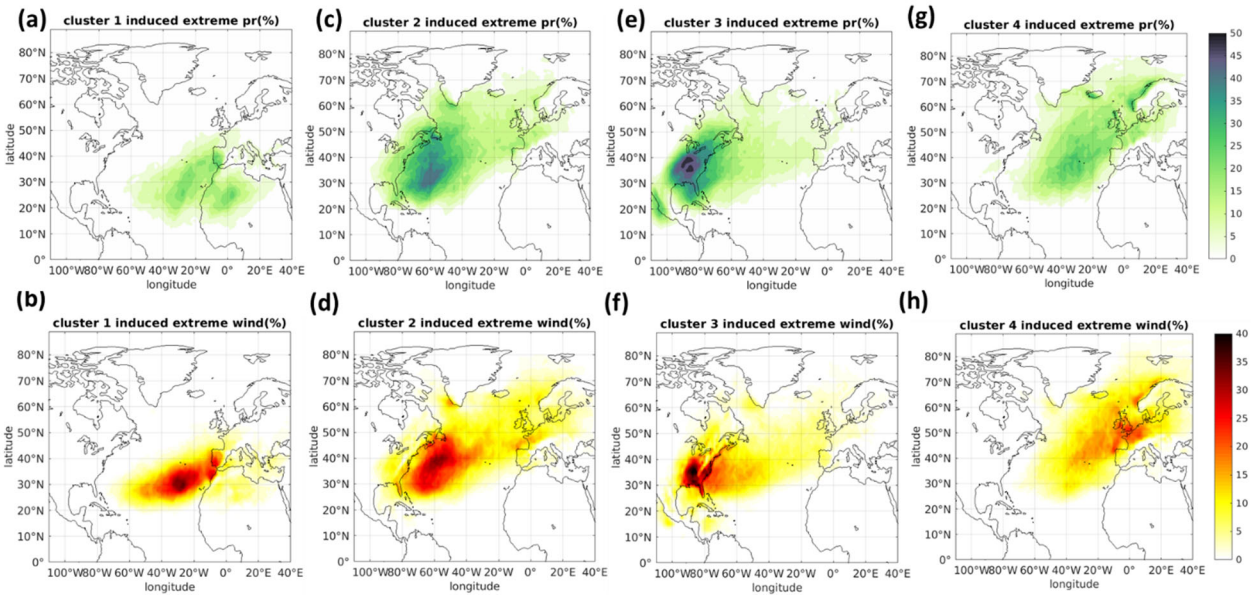

Figure 3.7 Extreme precipitation and winds that are associated with the four clusters. Frequency of extreme precipitation exceeding 98th percentile caused by (a) cluster 1, (c) cluster 2, (e) cluster 3, (f) cluster 4 (shaded, in %). Frequency of extreme wind caused by (b) cluster 1, (d) cluster 2, (f) cluster 3, and (h) cluster 4 (shaded, in %). Contour interval is 1%.

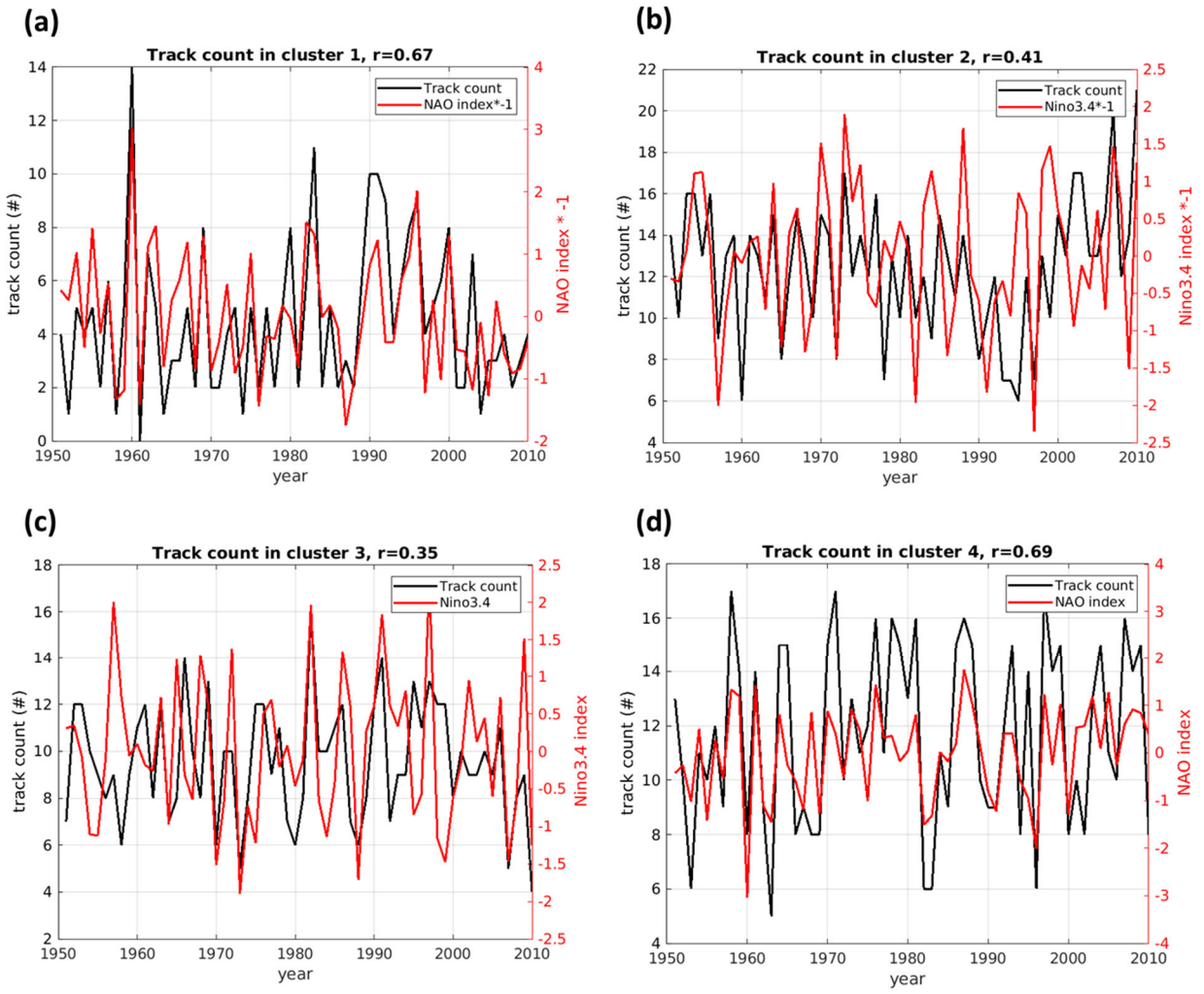

Figure S3.1 Time series of track count of the four clusters and large-scale climate indices. (a) Annual track count of cluster 1 (black line, in #) and standardized NAO index multiplied by -1 (red line, unitless). (b) Annual track count of cluster 2 (black line, in #) and standardized Niño 3.4 index multiplied by -1 (red line, unitless). (c) Annual track count of cluster 3 (black line, in #) and standardized Niño 3.4 index (red line, unitless). (d) Annual track count of cluster 4 (black line, in #) and standardized NAO index (red line, unitless). The y axes for black (red) lines are on the left (right). The correlation coefficient between the indices is indicated in the title of each subfigure.

CHAPTER 4: CONCLUSIONS AND FUTURE DIRECTION

Conclusions

Chapter 1 provides a broad review on the documented atmospheric river (AR) studies and a summary of the motivation of this thesis.

In Chapter 2, the sea surface temperature (SST)-forced interannual variability in cold-season (DJFM) ARs over the North Atlantic (NA) and its links to large-scale climatic circulations are examined using an ensemble of 30 simulations with a high-resolution atmospheric general circulation model (AGCM) over the period from year 1951 to 2011. An empirical orthogonal function (EOF) analysis is performed to AR occurrence, and the three leading modes (EOF1-EOF3) altogether explain 80% of the total interannual variability. EOF1 is a north-south wobbling pattern roughly modulated by linearly combined positive El Niño-Southern Oscillation (ENSO) and negative North Atlantic Oscillation (NAO) indices. Co-existing El Niño conditions and negative polarity of NAO reinforce each other in their correspondent water vapor and low-level wind fields, shifting ARs equatorward, while La Niña events and concurrent positive NAO shift ARs poleward. In EOF2, a meridional concentration and dispersion of AR occurrence at basin scale is primarily linked to Scandinavian pattern and secondarily to easternmost tropical Pacific SST anomalies. EOF3 is characterized by a positive anomaly over the Atlantic margin and off the coast of northern Europe, and PC3 has a significant upward trend over the study period. It is mainly governed by a linear superposition of ENSO and NAO, both in their positive manner, with ENSO shaping the

distribution of water vapor and NAO contributing to atmospheric circulation. The underlying upward trend is suggested to connect with the substantial Indo-west Pacific warming since 1970s. ARs over central to eastern U.S. are found to have higher predictability under the forcing of ENSO, while the inherent stochastic variability associated with NAO introduces a high level of unpredictability to ARs over western Europe.

In Chapter 3, a curve clustering method is employed to group DJFM AR tracks in the first member of an ensemble simulations (M01) and the Japanese 55-year reanalysis (JRA-55) into four distinct clusters. The climatology and four individual clusters in M01 all remarkably resemble those in JRA-55. Each cluster impacts a different region of NA. In M01, tracks in cluster 1 with the lowest track density, weakest intensity and shortest duration are governed by a negative polarity of NAO, making landfall to western Iberian Peninsula, Mediterranean Sea, and northwestern Africa. cluster 2 is correlated with negative SST anomalies in ENSO regions, namely La Niña conditions, with most impacts located over the open ocean off the U.S. east coast. Cluster 3 has the highest track density, impacting central-to-eastern U.S. during El Niño episodes. Cluster 4 is regulated by a positive phase of NAO and negative PNA pattern, striking northwestern Europe. The overall AR tracks identified in M01 account for over 80% (70%) of the extreme precipitation (winds) along the east coast of North America, with cluster 3 contributing to the largest portion of the percentage. Cluster 1 is responsible for about 25% of the extreme precipitation and winds over the Iberian Peninsula, and more than 25% of the extreme rainfall and winds along the Atlantic margin of northern Europe are subject to cluster 4.

Future direction

A future direction of AR studies is the projected changes in AR occurrence and tracks under global warming. Water vapor content in the atmosphere is projected to increase due to global warming, thus causing the magnitude of most extreme ARs to intensify and the number to increase in NA (Lavers et al. 2013; Ramos et al. 2016). A global study shows that, by comparing historical runs and representative concentration pathways (RCPs) from the fifth Climate Model Intercomparison Project (CMIP5), Integrated water vapor transport (IVT) calculated from RCP8.5 scenario is also found to increase by 30-40% in the North Pacific and NA (Lavers et al. 2015). This projected increase in IVT further supports an intensification and growing numbers of ARs since IVT is one of the key criteria to identify an AR. Another comparison between historical run and projected A2 emission scenario from seven Intergovernmental Panel on Climate Change (IPCC) GCMs reveals that years with more ARs become more frequent, while average occurrence of ARs barely changes. Also, the same pattern is found in AR intensity that the extreme instead of mean value is projected to increase by the end of 21st century (Dettinger 2011). A common belief among these studies is that the thermodynamic response to global warming, namely, enhanced water vapor content in the atmosphere, is the dominating factor for future changes in ARs (Ramos et al. 2016; Lavers et al. 2015; Lavers et al. 2013). This future increase in AR intensity and occurrence is expected to result in higher risks of floods and extreme precipitation due to the robust relationships between ARs and these disasters. However, some heterogeneities in projected changes were found among regions affected by ARs due to model uncertainties. For example, ARs landfalling on west coast of United States are projected to shift equatorward in response to the subtropical jet shift in winter, whereas ARs over U.K. are dominated by eddy-driven jet and will experience a modest change in frequency in winter and increased frequency in transition seasons

(Shields and Keihl 2016). Another direction is the subseasonal-to-seasonal predictions of ARs (DeFlorio et al. 2019a, 2019b). Both a reasonable long-term projection and an accurate subseasonal-to-seasonal prediction of AR activities (e.g. occurrence, intensity and trajectory) can provide instructions on policy making, hazard control and water resources management, and thus are hotspots among AR research topics.

REFERENCES

Bao, J.-W., S. A. Michelson, P. J. Neiman, F. M. Ralph, and J. M. Wilczak, 2006: Interpretation of enhanced integrated water vapor bands associated with extratropical cyclones: Their formation and connection to tropical moisture. Mon. Wea. Rev., 134, 1063–1080, doi:10.1175/MWR3123.1.

Barth, N. A., G. Villarini, M. A. Nayak, and K. White, 2017: Mixed populations and annual flood frequency estimates in the western United States: The role of atmospheric rivers, Water Resour. Res., 53, 257–269, doi:10.1002/2016WR019064.

Bell, C. J., L. J. Gray, A. J. Charlton-Perez, M. M. Joshi, and A. A. Scaife, 2009: Stratospheric communication of El Niño teleconnections to European winter. J. Climate, 22, 4083–4096, https://doi.org/10.1175/2009JCLI2717.1.

Brands, S., J. M. Gutiérrez, and D. San-Martín, 2017: Twentieth century atmospheric river activity along the west coasts of Europe and North America: Algorithm formulation, reanalysis uncertainty and links to atmospheric circulation patterns. Climate Dyn., 48, 2771–2795, doi:10.1007/s00382-016-3095-6

Brönnimann, S., 2007: Impact of El Niño–Southern Oscillation on European climate. Rev. Geophys., 45, RG3003, doi:10.1029/ 2006RG000199.

Camargo, S. J., A. W. Robertson, S. J. Gaffney, P. Smyth, and M. Ghil, 2007: Cluster analysis of typhoon tracks. Part I: general properties. J. Climate, 20, 3635–3653.

Cassou, C., and L. Terray, 2001: Ocean forcing of the wintertime low-frequency atmospheric variability in the North Atlantic European sector: A study with the ARPEGE model. J. Climate, 14, 4266–4291, https://doi.org/10.1175/1520-0442(2001)014<4266:OFOTWL>2.0.CO;2.

Chu, C., X.-Q. Yang, X. Sun, D. Yang, Y. Jiang, T. Feng, and J. Liang, 2017: Effect of the tropical Pacific and Indian Ocean warming since the late 1970s on wintertime Northern Hemispheric atmospheric circulation and East Asian climate interdecadal changes. Climate Dyn., 10.1007/s00382-017-3790-y, 50, 7-8, (3031-3048).

Cohen, J., A. Frei, and R. Rosen, 2005: Evaluation of the role of boundary conditions in AMIP-2 simulations of the NAO. J. Climate, 18, 973–981, doi:10.1175/JCLI-3305.1.

Cordeira, J. M., J. Stock, M. D. Dettinger, A. M. Young, J. F. Kalansky, and F. M. Ralph, 2019: A 142-year climatology of Northern California landslides and atmospheric rivers. Bull. Am. Meteorol. Soc. https://doi.org/10.1175/BAMS-D-18-0158.1.

Czaja, A., and C. Frankignoul, 2002: Observed impact of Atlantic SST anomalies on the North Atlantic Oscillation. J.Climate, 15, 606–623,doi:https://doi.org/10.1175/1520-0442(2002)015<0606:OIOASA>2.0.CO;2.

DeFlorio, M. J., D. E. Waliser, F. M. Ralph, B. Guan, A. Goodman, P. B. Gibson, et al., 2019: Experimental subseasonal-to-seasonal (S2S) forecasting of atmospheric rivers over the western United States, J. Geophys. Res. Atmos., 124, 11242–11265, doi:10.1029/2019JD031200.

DeFlorio, M. J., D. E. Waliser, B. Guan, F. M. Ralph, and F. Vitart, 2019: Global evaluation of atmospheric river subseasonal prediction skill, Clim. Dyn., 52, 3039–3060, doi:10.1007/s00382-018-4309-x.

Dettinger, M., 2011: Climate change, atmospheric rivers, and floods in California—A multimodel analysis of storm frequency and magnitude changes. J. Amer. Water Resour. Assoc., 47, 514–523, doi:https://doi.org/10.1111/j.1752-1688.2011.00546.x.

——, 2013: Atmospheric rivers as drought busters on the U.S. West Coast. J. Hydrometeor., 14, 1721–1732, https:// doi.org/10.1175/JHM-D-13-02.1.

Eiras-Barca J, Brands S, Miguez-Macho G, 2016: Seasonal variations in North Atlantic atmospheric river activity and associations with anomalous precipitation over the Iberian Atlantic Margin. J Geophys Res. doi: 10.1002/2015JD023379.

Gaffney, S. J., Robertson, A. W., Smyth, P., Camargo, S. J. & Ghil, M. Probabilistic clustering of extratropical cyclones using regression mixture models. Clim. Dyn. 29, 423–440 (2007).

Gershunov, A., T. Shulgina, F. M. Ralph, D. A. Lavers, and J. J. Rutz, 2017: Assessing the climate-scale variability of atmospheric rivers affecting western North America. Geophys. Res. Lett., 44, 7900–7908. https://doi.org/10.1002/2017GL074175

Gouirand, I., and V. Moron, 2003: Variability of the impact of El Niño–Southern Oscillation on sea-level pressure anomalies over the North Atlantic in January to March (1874–1996). Int. J. Climatol., 23, 1549–1566, https://doi.org/10.1002/joc.963.

Greatbatch, R. J., J. Lu, and K. A. Peterson, 2004: Nonstationary impact of ENSO on Euro-Atlantic winter climate. Geophys. Res. Lett., 31, L02208, https://doi.org/10.1029/2003GL018542.

Guan, B., N. P. Molotch, D. E. Waliser, E. J. Fetzer, and P. J. Neiman, 2010: Extreme snowfall events linked to atmospheric rivers and surface air temperature via satellite measurements. Geophys. Res. Lett., 37, L20401, doi:https://doi.org/10.1029/2010GL044696.

——, N. P. Molotch, D. E. Waliser, E. J. Fetzer, and P. J. Neiman, 2013: The 2010/2011 snow season in California's Sierra Nevada: Role of atmospheric rivers and modes of large-scale variability. Water Resour. Res., 49, 6731–6743, doi:10.1002/wrcr.20537.

——, and D. E. Waliser, 2015: Detection of atmospheric rivers: Evaluation and application of an algorithm for global studies. J. Geophys. Res. Atmos., 120, 12 514–12 535, https://doi.org/10.1002/2015JD024257.

——, and D. E. Waliser, 2019: Tracking Atmospheric Rivers Globally: Spatial Distributions and Temporal Evolution of Life Cycle Characteristics. Journal of Geophysical Research: Atmospheres,124,12,523–12,552. https://doi.org/10.1029/2019JD031205

Highland, L. M., 2004: Landslide types and processes. USGS Fact Sheet 2004-3072, 4 pp., https://doi.org/10.3133/fs20043072.

Hirahara, S., M. Ishii, and Y. Fukuda, 2014: Centennial-scale sea surface temperature analysis and its uncertainty. J. Climate, 27, 57–75, doi:https://doi.org/10.1175/JCLI-D-12-00837.1.

Hoerling, M. P., J. W. Hurrell, and T. Xu, 2001: Tropical origins for recent North Atlantic climate change. Science, 292, 90–92.

——, J. W. Hurrell, T. Xu, G. T. Bates and A. S. Phillips, 2004: Twentieth century North Atlantic climate change. Part II: understanding the effect of Indian Ocean warming. Clim. Dyn., 23, 391–405.

Horel, J. D., and J. M. Wallace, 1981: Planetary-scale atmospheric phenomena associated with the Southern Oscillation. Mon. Wea. Rev., 109, 813–829.

Hoskins, B. J., I. N. James, and G. H. White, 1983: The shape, propagation and mean-flow interaction of large-scale weather systems. J. Atmos. Sci., 40, 1595–1612

Kamae, Y., W. Mei, S. -P. Xie, M. Naoi, and H. Ueda, 2017: Atmospheric rivers over the northwestern Pacific: Climatology and interannual variability. J. Climate, 30, 5605- 5619, doi.org/10.1175/JCLI-D-16-0875.1.

Khouakhi, A. and G. Villarini, 2016: On the relationship between atmospheric rivers and high sea water levels along the U.S. west coast. Geophys. Res. Lett. 43, 8815–8822.

Kim, H.-M., Y. Zhou, and M. A. Alexander, 2019: Changes in atmospheric rivers and moisture transport over the northeast Pacific and western North America in response to ENSO diversity. Climate Dyn., 52, 7375–7388, https://doi.org/10.1007/s00382-017-3598-9.

Klein, S. A., B. J. Soden, and N.-C. Lau, 1999: Remote sea surface temperature variations during ENSO: Evidence for a tropical atmospheric bridge. J. Climate, 12, 917–932, doi:https://doi.org/10.1175/1520-0442(1999)012<0917:RSSTVD>2.0.CO;2.

Knippertz, P., and H. Wernli, 2010: A Lagrangian climatology of tropical moisture exports to the Northern Hemispheric extratropics. J. Climate, 23, 987–1003, doi:10.1175/2009JCLI3333.1

Lavers, D. A., R. P. Allan, E. F. Wood, G. Villarini, D. J. Brayshaw, and A. J. Wade, 2011: Winter floods in Britain are connected to atmospheric rivers. Geophys. Res. Lett., 38, L23803, doi:10.1029/2011GL049783.

——, ——, ——, and A. J. Wade, 2012: The detection of atmospheric rivers in atmospheric reanalyses and their links to British winter floods and the large-scale climatic circulation. J. Geophys. Res., 117, D20106, doi:10.1029/2012JD018027.

——, ——, G. Villarini, B. Lloyd-Hughes, D. J. Brayshaw, and A. J. Wade, 2013: Future changes in atmospheric rivers and their implications for winter flooding in Britain. Environ. Res. Lett., 8, 034010, doi:10.1088/1748-9326/8/3/034010.

——, and G. Villarini, 2013: The nexus between atmospheric rivers and extreme precipitation across Europe. Geophys. Res. Lett., 40, 3259–3264, doi:https://doi.org/10.1002/grl.50636.

——, F. M. Ralph, D. E. Waliser, A. Gershunov, and M. D. Dettinger, 2015: Climate change intensification of horizontal water vapor transport in CMIP5. Geophys. Res. Lett., 42, 5617–5625, doi:https://doi.org/10.1002/2015GL064672.

Leung, L. R., and Y. Qian, 2009: Atmospheric rivers induced heavy precipitation and flooding in the western U.S. simulated by the WRF regional climate model. Geophys. Res. Lett., 36, L03820, doi:https://doi.org/10.1029/2008GL036445.

Li, Y. and N. Lau, 2012: Impact of ENSO on the Atmospheric Variability over the North Atlantic in Late Winter—Role of Transient Eddies. J. Climate, 25, 320–342, https://doi.org/10.1175/JCLI-D-11-00037.1

Mizuta, R., and Coauthors, 2012: Climate simulations using MRI-AGCM with 20-km grid. J. Meteor. Soc. Japan, 90A, 233–258, doi:https://doi.org/10.2151/jmsj.2012-A12.

——, and Coauthors, 2017: Over 5000 years of ensemble future climate simulations by 60-km global and 20-km regional atmospheric models. Bull. Amer. Meteor. Soc., https://doi.org/10.1175/BAMS-D-16-0099.1, in press.

Mundhenk, B. D., E. A. Barnes, and E. D. Maloney, 2016: All-season climatology and variability of atmospheric river frequencies over the North Pacific. J. Climate, 29, 4885–4903, doi:https://doi.org/10.1175/JCLI-D-15-0655.1.

Müller,W.A., and E.Roeckner, 2006: ENSO impact on midlatitude circulation patterns in future climate change projections. Geophys. Res. Lett., 33, L05711, doi:1029/2005GL025032.

Namias, J., 1939: The use of isentropic analysis in short term forecasting. J. Aeronaut. Sci. 6, 295–298. doi: 10.2514/8.860.

Neiman, P. J., F. M. Ralph, G. A. Wick, J. D. Lundquist, and M. D. Dettinger, 2008b: Meteorological characteristics and overland precipitation impacts of atmospheric rivers affecting the West Coast of North America based on eight years of SSM/I satellite observations. J. Hydrometeor., 9, 22–47, doi:https://doi.org/10.1175/2007JHM855.1.

——, L. J. Schick, and F. M. Ralph, 2011: Flooding in western Washington: The connection to atmospheric rivers. J. Hydrometeor., 12, 1337–1358, doi:https://doi.org/10.1175/2011JHM1358.1.

Orlanski, I., 1998: Poleward deflection of storm tracks. J. Atmos. Sci., 55, 2577–2602.

Payne, A. E., and G. Magnusdottir, 2014: Dynamics of landfalling atmospheric rivers over the North Pacific in 30 years of MERRA reanalysis. J. Climate, 27, 7133–7150, doi:10.1175/ JCLI-D-14-00034.1.

Pozo-Vázquez, D., M. J. Esteban-Parra, F. S. Rodrigo, and Y. Castro-Díez, 2001: The association between ENSO and winter atmospheric circulation and temperature in the North Atlantic region. J. Climate, 16, 3408–3420.

Ralph, F. M., P. J., Neiman, and G. A. Wick, 2004: Satellite and CALJET aircraftobservations of atmospheric rivers over the eastern North Pacificocean during the winter of 1997/98. Mon. Wea. Rev. 132, 1721–1745. doi: 10.1175/1520-0493(2004)132<1721:SACAOO>2.0.CO;2.

——, ——, and R. Rotunno, 2005: Dropsonde Observations in Low-Level Jets over the Northeastern Pacific Ocean from CALJET-1998 and PACJET-2001: Mean Vertical-Profile and Atmospheric-River Characteristics. Mon. Wea. Rev. 133, 889–910. doi: 10.1175/MWR2896.1.

——, ——, G. A. Wick, S. I. Gutman, M. D. Dettinger, D. R. Cayan, and A. B. White, 2006: Flooding on California's Russian River: Role of atmospheric rivers. Geophys. Res. Lett., 33, L13801, doi:https://doi.org/10.1029/2006GL026689.

——, and M. D. Dettinger, 2011: Storms, floods, and the science of atmospheric rivers. Eos Transactions American Geophysical Union, 92(32), 265–266. https://doi.org/10.1029/2011EO320001.

——, and Coauthors, 2017b: Dropsonde observations of total integrated water vapor transport within North Pacific atmospheric rivers. J. Hydrometeor., 18, 2577–2596, https://doi.org/ 10.1175/JHM-D-17-0036.

Ramos, A. M., R. Tomé, R. M. Trigo, M. L. R. Liberato, and J. G. Pinto, 2016b: Projected changes in atmospheric rivers affecting Europe in CMIP5 models, Geophys. Res. Lett., 43, 9315–9323, https://doi.org/10.1002/2016GL070634.

Rasmusson, E. M., and K. Mo, 1993: Linkages between 200-mb tropical and extratropical circulation anomalies during the 1986–1989 ENSO cycle. J. Climate, 6, 595–616.

Ridder, N., H. de Vries, and S. Drijfhout, 2018: The role of atmospheric rivers in compound events consisting of heavy precipitation and high storm surges along the Dutch coast, Nat. Hazards Earth Syst. Sci., 18, 3311–3326, https://doi.org/10.5194/nhess-18-3311-2018.

Rogers, J. C., 1984: The association between the North Atlantic Oscillation and the Southern Oscillation in the Northern Hemisphere. Mon. Wea. Rev., 112, 1999–2015, doi:10.1175/ 1520-0493(1984)112,1999:TABTNA.2.0.CO;2.

Rutz J, C. Shields, J. M. Lora, A. E. Payne , B. Guan, P.A. Ullrich, T. O'Brien, R. Leung, F. M. Ralph, M. Wehner, S. Brands, A. Collow, A. Gershunov, N. Goldenson, I. Gorodetskaya, H. Griffith, S. Hagos,

K. Kashinath, B. Kawzenuk, H. Krishnan, D. Lavers, G. Magnusdottir, P. Nguyen, Prabhat, A. Ramos, S. Sellars, T. Tomé, D. Walister, D. Walton, G. Wick, A. Wilson, M. Viale, 2019: The Atmospheric River Tracking Method Intercomparison Project (ARTMIP): quantifying uncertainties in atmospheric river climatology. J Geophys Res Atm. https://doi.org/10.1029/2019JD030936.

Ryoo, J.-M., D. E. Waliser, D. W. Waugh, S. Wong, E. J. Fetzer, and I. Fung, 2015: Classification of atmospheric river events on the U.S. West Coast using a trajectory model. J. Geophys. Res. Atmos., 120, 3007–3028, doi:https://doi.org/10.1002/2014JD022023.

Sanchez-Gomez, E., C. Cassou, D. L. R. Hodson, N. Keenlyside, Y. Okumura, and T. Zhou, 2008: North Atlantic weather regimes response to Indian–western Pacific Ocean warming: A multi-model study. Geophys. Res. Lett., 35, L15706, doi:10.1029/2008GL034345.

Seiler, C., and F. W. Zwiers, 2016b: How well do CMIP5 climate models reproduce explosive cyclones in the extratropics of the Northern Hemisphere? Climate Dyn., 46, 1241–1256, https://doi.org/10.1007/s00382-015-2642-x.

Shields, C. A., and J. T. Kiehl, 2016: Atmospheric river landfalllatitude changes in future climate simulations. Geophys. Res. Lett., 43, 8775–8782, https://doi.org/10.1002/2016GL070470.

——, J. J. Rutz, L.-Y. Leung, F. M. Ralph, M. Wehner, B. Kawzenuk, J. M. Lora, E. McClenny, T. Osborne, A. E. Payne, P. Ullrich, A. Gershunov, N. Goldenson, B. Guan, Y. Qian, A.M. Ramos, C. Sarangi, S. Sellars, I. Gorodetskaya, K. Kashinath, V. Kurlin, K. Mahoney, G. Muszynski, R. Pierce, A. C. Subramanian, R. Tome, D. Waliser, D. Walton, G. Wick, A. Wilson, D. Lavers, Prabhat, A. Collow, H. Krishnan, G. Magnusdottir, and P. Nguyen, 2018: Atmospheric River Tracking Method Intercomparison Project (ARTMIP): project goals and experimental design, Geosci. Model Dev., 11, 2455–2474, https://doi.org/10.5194/gmd-11-2455-2018.

Strong, C., and G. Magnusdottir, 2008a: How Rossby wave breaking over the Pacific forces the North Atlantic Oscillation. Geophys. Res. Lett., 35, L10706, doi:10.1029/2008GL033578.

——, and ——, 2008b: Tropospheric Rossby wave breaking and the NAO/NAM. J. Atmos. Sci., 65, 2861–2876, doi:10.1175/ 2008JAS2632.1

Tan, Y., F. Zwiers, S. Yang, C. Li, and K. Deng, 2020: The role of circulation and its changes in present and future atmospheric rivers over western North America. J. Climate, 33, 1261–1281, https://doi.org/10.1175/JCLI-D-19-0134.1.

Toniazzo, T., and A. A. Scaife, 2006: The influence of ENSO on winter North Atlantic climate. Geophys. Res. Lett., 33, L24704, doi:10.1029/2006GL027881.

Waliser, D. E., and B. Guan, 2017: Extreme winds and precipitation during landfall of atmospheric rivers. Nat. Geosci., 10, 179–183, https://doi.org/10.1038/ngeo2894.

Wu, A., and Hsieh, W. W., 2004: The nonlinear Northern Hemisphere winter atmospheric response to ENSO, Geophys. Res. Lett., 31, L02203, doi:10.1029/2003GL018885.

Zhang, W., and G. Villarini, 2018: Uncovering the role of the East Asian jet stream and heterogeneities in atmospheric rivers affecting the western United States. Proc. Natl. Acad. Sci. USA, 115, 891–896, https://doi.org/10.1073/pnas.1717883115.

Zhu, Y., and R. E. Newell, 1998: A proposed algorithm for moisture fluxes from atmospheric rivers. Mon. Wea. Rev., 126, 725–735, doi:10.1175/1520-0493(1998)126,0725: APAFMF.2.0.CO;2.